In compliance with the
Canadian Privacy Legislation
some supporting forms
may have been removed from
this dissertation.

While these forms may be included
in the document page count,
their removal does not represent
any loss of content from the dissertation.

University of Alberta

Fabrication of Biochips with Integrated Micro-optics and Microfluidics

By

Hong Qiao

A thesis submitted to the Faculty of Graduate Studies and Research in partial fulfillment of the requirements for the degree of **Master of Science**.

Department of Electrical and Computer Engineering

Edmonton, Alberta

Fall, 2003

National Library of Canada
Bibliothèque nationale du Canada

Acquisitions and Bibliographic Services
Acquisisitons et services bibliographiques

395 Wellington Street
Ottawa ON K1A 0N4
Canada

395, rue Wellington
Ottawa ON K1A 0N4
Canada

Your file Votre référence
ISBN: 0-612-87864-3
Our file Notre référence
ISBN: 0-612-87864-3

The author has granted a non-exclusive licence allowing the National Library of Canada to reproduce, loan, distribute or sell copies of this thesis in microform, paper or electronic formats.

The author retains ownership of the copyright in this thesis. Neither the thesis nor substantial extracts from it may be printed or otherwise reproduced without the author's permission.

L'auteur a accordé une licence non exclusive permettant à la Bibliothèque nationale du Canada de reproduire, prêter, distribuer ou vendre des copies de cette thèse sous la forme de microfiche/film, de reproduction sur papier ou sur format électronique.

L'auteur conserve la propriété du droit d'auteur qui protège cette thèse. Ni la thèse ni des extraits substantiels de celle-ci ne doivent être imprimés ou aturement reproduits sans son autorisation.

Canada

University of Alberta

Library Release Form

Name of Author: Hong Qiao

Title of Thesis: Fabrication of Biochips with Integrated Micro-optics and Microfluidics

Degree: Master of Science

Year this Degree Granted: 2003

Permission is hereby granted to the University of Alberta Library to reproduce single copies of this thesis and to lend or sell such copies for private, scholarly or scientific research purposes only.

The author reserves all other publication and other rights in association with the copyright in the thesis, and except as herein before provided, neither the thesis nor any substantial portion thereof may be printed or otherwise reproduced in any material from whatever without the author's prior written permission.

Date: Sep. 19, 2003

University of Alberta

Faculty of Graduate Studies and Research

The undersigned certify that they have read, and recommend to the Faculty of Graduate Studies and Research for acceptance, a thesis entitled **Fabrication of Biochips with Integrated Micro-optics and Microfluidics** submitted by **Hong Qiao** in partial fulfillment of the requirement for the degree of **Master of Science**.

Date: Aug. 15, 2003.

ABSTRACT

An integrated optical biochip has been developed by fabricating ion-exchange waveguides for the optical system and etching microchannels as the microfluidics system on a single glass substrate. The process descriptions of dry film field-assisted ion-exchange waveguides, glass-etched microchannels, and bonding of the biochips are presented, and the fabrication problems along with their solutions are discussed. The relations of ion-exchange parameters, the resulting ion-exchange currents and waveguide depths, and the evaluation of the waveguide properties including waveguide losses are presented. Two methods are described to integrate waveguides and microchannels on a single substrate. The feasibility of the integration is demonstrated by detecting the fluorescence signals from a dyed fluid in an integrated optical biochip.

For mom & DOC

ACKNOWLEDGEMENTS

I would like to express my deepest gratitude and appreciation to my supervisor, Dr. James N. McMullin, for introducing me into this exiting and challenging field and guiding me throughout this research. I extend special gratitude to Dr. Sandy M. Robinson for accommodating me in a pleasant working environment, and Dr. Mark R. Freeman and Dr. Norman Beaulieu for being on my committee.

I would like to express my sincere thanks to former and current group members in Dr. McMullin's and Dr. Robinson's labs, especially Armin Grundmann for teaching me the ion-exchange techniques, Sanket Goel and Angela Antoniu for cooperating in microfluidics experiments, and Dr. Keith B. Brown, Dr. Dexin Lu, Xiaohong Quan, Dean Spicer, and Dr. Gunter and Marli Schmidt-Weinmar for their professional and personal advice.

I am grateful for the staff of the Micromechaning and Nanofabrication Facility (NanoFab), in particular, Dr. Ken Westra, Stephanie Bozic, Dione Chambers and Dr. Mirwais Aktary, for their significant and concrete technical assistance. I would also like to thank Dr. Justine Taylor in the Chemistry Department at University of Alberta and Dr. Yuebin Ning from Norcada Inc. of Edmonton for sharing their expertise in the bonding of glass. Many thanks to John Crabtree, Herb Hartshorne, and Gregory Nilsson of Micralyne Inc. of Edmonton and Harini Gopaluni, P. Nakeeran and Robert Bryce of the TRLabs for offering the facility's support and cooperation. My appreciation is also extended to Herbert Dexel and Barry Arnold in the machine shop of the Department of Electrical and Computer Engineering for the quality of their support services, and George Braybrook and Dr. Dong-chen Lee in the Department of Earth and Atmospheric Sciences for taking SEM photographs.

I would like to acknowledge the Canadian Institute for Photonic Innovations (CIPI), the Natural Science and Engineering Research Council of Canada (NSERC), and Micralyne Inc. of Edmonton for the financial support.

My sincere thanks to my Canadian family, Susanne Erfani, Nina Erfani and Kevin Moore for their consistent encouragement and help on the language.

Finally, I will forever be grateful to my parents and my fiancé, who have always been there for me no matter whether I am up or down.

TABLE OF CONTENTS

1	**Introduction**	**1**
	1.1 Biochips	1
	1.1.1 Current state of integrated optical biochips	2
	1.2 Overall research theme	4
	1.2.1 PMT detection system	5
	1.2.2 Microparticle detection in biochips	6
	1.3 Outline of this research	9
2	**Fabrication of Traditional Biochips**	**11**
	2.1 Introduction	11
	2.2 Process summary of fabricating microchannels	11
	2.3 Processing issues	14
	2.3.1 Glass metallization	14
	2.3.2 Bonding and cleaning	15
	2.3.3 Microchannel etching results	16
3	**Fabrication and Characterization of Ion-exchange Waveguides**	**18**
	3.1 Introduction	18
	3.1.1 Ion-exchange mechanisms	18
	3.1.2 Fabrication methods	19
	3.1.3 Substrate selection	22
	3.2 Fabrication of ion-exchange waveguides	23
	3.3 Processing issues in waveguide fabrication	25
	3.3.1 Ion-exchange mask	25
	3.3.2 Waveguide coloration	28
	3.4 Relations of ion-exchange parameters and results	30
	3.4.1 Ion-exchange parameters and currents	30
	3.4.2 Currents and waveguide depths	32
	3.5 Characterizations of ion-exchange waveguides	35
	3.5.1 Waveguide side diffusions and surface swells	35
	3.5.2 Waveguide losses	39

4 Biochips with Integrated Microchannels and Waveguides 44

4.1 Integration of microchannels and waveguides on a single substrate: two approaches 44

4.1.1 Fabrication of waveguides on a substrate with microchannels 44

4.1.2 Fabrication of microchannels on a substrate with waveguides 47

4.1.3 Alignment of waveguides and microchannels 53

4.2 Completion of integrated biochips 54

4.2.1 Interaction of the bonding process and waveguides 54

4.3 Detection of fluorescence in integrated optical biochips 56

5 Conclusions 59

References 61

Appendix 1: Procedure of Fabricating Microchannels 65

Appendix 2: Procedure of Fabricating Ion-exchange Waveguides 74

Appendix 3: A Dual Functional Mask Layout 80

LIST OF FIGURES

Figure 1-1 A commercial biochip made by Micralyne Inc. of Edmonton, Alberta, Canada, its size compared with a penny. 1

Figure 1-2 (a) Laser-written crossed channel system with a glass lid. Circle at left is a reservoir for introducing fluid samples. (b) Laser-written channel walls (horizontal) and an intersecting waveguide (vertical), the channel walls are in 100-200μm scale. 3

Figure 1-3 A view on three scales of the research at our lab. 4

Figure 1-4 PMT setup and computer control system 6

Figure 1-5 Simplified scheme of the microparticle fluorescence detection setup. 7

Figure 1-6 (a) Microparticle detection with an innovated launch-and-detect (LAD) detector. (b) Top view of the LAD detector under a microparticle in a microchannel. The microparticale is at the center boundary of the two fibers. 9

Figure 2-1 Approximate cross-section of a Micalyne biochip. 11

Figure 2-2 Microchannels etched in the NanoFab. (a) Mask lifting around a 10 μm channnel during glass etching. (b) Spikes-shape etching on the channel walls. 15

Figure 2-3 SEM image of a cross-section of a 28-μm-deep 86-μm-wide microchannel. 17

Figure 2-4 Undercutting of the isotropic glass etching and lateral expanding of the microchannel mask opening. 17

Figure 3-1 (a) Schematic diagram of ion exchange in a $AgNO_3$ bath. (b) Thermal diffusion is accelerated with an electric field applied in $AgNO_3$ baths. 20

Figure 3-2 (a) Schematic diagram of dry film field-assisted ion exchange. (b) Electric field in glass sovled in [17] for dry film field-assisted ion exchange. 21

Figure 3-3 SEM iamge of waveguides using a Cr mask. 26

Figure 3-4 (a) Profilometer plot of a 20 μm mask opening after heating in a furnace. (b) Rough waveguide made with the mask opening with the profile in Figure 3-4(a). (c) Profilometer plot of a 20 μm mask opening smoothed by an additional cool piranha bath after heating in a furnace. (d) Smooth waveguide made with the mask opening with the profile in Figure 3-4(c). 28

Figure 3-5 A section of a waveguide splitter. The dark lines in the center of the waeguides are the mask opening area and have visibly yellow color indicating the presence of Ag atoms. 30

Figure 3-6 Current profiles vs. time on three identical substrates using different parameters. 31

Figure 3-7 Current vs.Temperature at E=100V/mm on five Corning 0211 substrates with the same diffusion area. The data is approximated very well by an exponential curve. 31

Figure 3-8 Linear relation of current with the electric field at T=360°C on five Corning 0211 substrates with the same diffusion area. 32

Figure 3-9 Evaluation of waveguide profile *d(y)* and source film thickness *s(y)* during ion-exchange in Ref. [19]. Each *d(y)* curve corresponds to one *s(y)* curve. 35

Figure 3-10 (a) SEM image of a channel waveguide. The stripe on the center top of the waveguide is where the mask opening was. The size of side diffusion is approximately the depth of the waveguide. (b) Substrate surface changed by the ion exchange in the mask opening area 36

Figure 3-11 (a) SEM Image of a waveguide made on Schott borofloat glass with a 21 μm opening. (b) SEM image of a waveguide made on Corning 0211 glass with a 21 μm opening. 37

Figure 3-12 (a) Profilometer plot of a 130 nm swell of a 32 μm deep waveguide on a Corning 0211 substrate. (b) Profilometer plot of a 60 nm swell of a 36 um deep waveguide on a Schott borofloat substrate. 38

Figure 3-13 (a) Top view of laser light propagating in a 4-cm-long waveguide. An optical fiber is coupled to the waveguide from the left. (b) Side view of laser light at a waveguide end. 40

Figure 3-14 Schematic setup of waveguide propagation loss measurement. 41

Figure 3-15 Measurement of scattered light at 1 mm intervals with waveguide facing up. Vertical units are 10log(PMT signal in mV). The data, except the first and last 5 mm are fitted into a line. Attenuation is 3.4 dB/cm. 42

Figure 3-16 Measurement of scattered light at 1 mm intervals with waveguide facing down. Vertical units are 10log(PMT signal in mV). The data except the first and last 5 mm are fitted into a line. Attenuation is 2.4 dB/cm. 42

Figure 3-17 Measurement of scattered light across a waveguide. 43

Figure 4-1 Intersection pictures of microchannel walls (vertical dark strips) and waveguide patterns (horizontal strips). (a) No photoresist on the surface close to the microchannel. Photoresis on the left side of the channel is thicker than that on the right side. (b) Cr (white) on the surface close to the microchannel is etched. Cr at the intersection is not etched completely. 46

Figure 4-2 SEM image of 50-μm-deep ion-exchange at a 20-μm-deep channel bottom. 47

Figure 4-3 Optical profilometer scanning of a bulge at the intersection of a 28-μm-deep microchannel and an 86-μm-wide 36-μm-deep waveguide. 48

Figure 4-4 SEM images of trenches formed at an intersection. (a) microchannel (vertical) and waveguide (horizontal). (b) microchannel (horizontal) and waveguide (vertical). 49

Figure 4-5 (a) Trenches occur when the curved channel is etched into the ion-exchange mask opening area.(b) No trench occurs when the curved channel is not etched into the ion-exchange mask opening area. 50

Figure 4-6 Proposed intersection scheme to avoid trenches etched in the waveguides. 51

Figure 4-7 BPM simulations in Ref. [9] of light from a 24-μm-wide waveguide (4 μm high) coupled into a 500-μm-wide channel through a 10-μm-wide dike. 52

Figure 4-8 Picture of three-group alignment marks diffused into one corner of the substrate. 54

Figure 4-9 SEM image of a waveguide after bonding. 55

Figure 4-10 Diffusion into the cover plate in the mask opening area during bonding. 56

Figure 4-11 Optical tests on integrated biochips. (a) Laser light travels in a Y-shape waveguide and shines into a straight microchannel. (b) Laser light travels in a curved waveguide and shines into a U-shape microchannel. 57

Figure 4-12 PMT measurements at intersections of waveguides and microchannels when the microchannel was empty and injected with a dye solution. 58

LIST OF SYMBOLS

Ag	silver
Ag_2O	silver oxide
$AgNO_3$	silver nitrate
Al	aluminum
As_2O_3	arsenic oxide
Au	gold
Cr	chromium
Cr_2O_3	chromium oxide
Cs	cesium
CsCl	cesium chloride
$CsNO_3$	cesium nitrate
FeO	iron oxide
H_2O_2	hydrogen peroxide
H_2SO_4	sulfuric acid
He-Ne	helium-neon
HF	hydrofluoric acid
HI	hydroiodide acid
K	potassium
KI	potassium iodide
KNO_3	potassium nitrate
Li	lithium
N_2	nitrogen
Na	sodium
Rb	rubidium
Sb_2O_3	antimony oxide
Si	silicon
SiO_2	silicon dioxide
Ti	titanium
Tl	thallium
$TlNO_3$	thallium nitrate

List of Abbreviations

μm	micrometer
μ-TAS	micro-total-analysis system
BPM	beam-propagation method
CCD	charge coupled device
cm	centimeter
dB	decibel
DI	de-ionized
FWHM	full width half maximum
IPA	isopropyl alcohol
LAD	launch-and-detect
mA	Milliampere
MEMS	micro-electro-mechanical system
min	minute
mm	millimeter
mV	millivolt
NanoFab	Micromechaning and Nanofabrication Facility
nm	nanometer
NOAs	Norland optical adhesives
°C	degree celsius
PDMS	polydimethylsiloxane
PMT	phtomultiplier tube
Ref.	reference
RF	radio frequency
SEM	scanning electron microscope
UV	ultraviolet
V	volt

1 INTRODUCTION

1.1 Biochips

Biochips are substrates with imbedded micrometer-scale channels, in which small fluid samples can be studied. Biochips have been developed for such applications as microparticle detection and fluorescence identification of microparticle types, blood cell studies, on-chip biological and genetic analysis, drug discovery, and environmental pollution tests [1][2][3]. Generally, they are candidates for any sensor application where a small fluid or even gaseous sample is involved. A commercial biochip by Micralyne Inc. of Edmonton, Canada is shown in Figure 1-1.

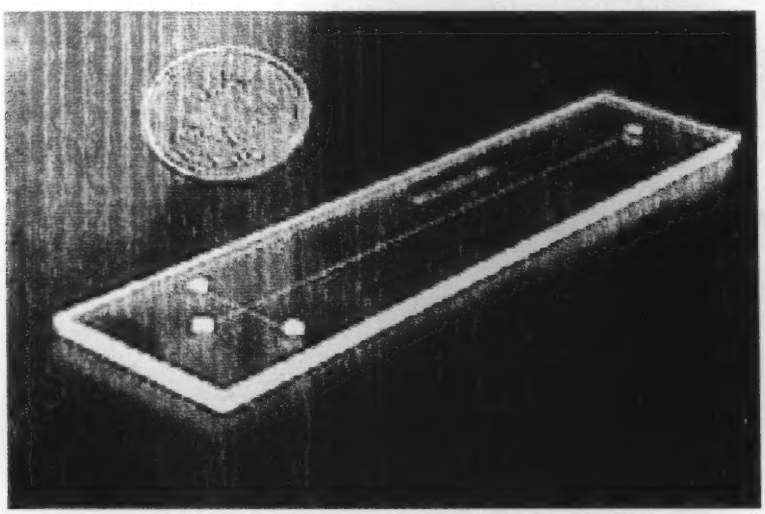

Figure 1-1 A commercial biochip made by Micralyne Inc. of Edmonton, Alberta, Canada, its size compared with a penny.

Biochips are usually fabricated utilizing micro-electro-mechanical system (MEMS) technologies on glass, silicon (Si), or polymer substrates. The methods to make microchannels on a biochip include glass wet etching, (such as Micralyne biochips), deep plasma silicon etching [4][5], UV-exposed epoxy [6], and recently polydimethylsiloxane (PDMS) casting [7].

A new area of biochip research is to fabricate micrometer-scale waveguides in biochips. The goal is to launch incident light into the waveguides, deliver the light to specific points in microchannels, capture characteristic signals and use other waveguides to deliver these signals to on-chip or off-chip detectors. As a result, portable micro-total-analysis systems (μ-TAS) could be realized that would utilize optical interrogation without large and expensive bulk optics and intensive operator involvement. Also, simultaneous detection of multi-position on a biochip is possible. Compared to traditional biochips with only microchannels, we call biochips with waveguides "integrated optical biochips" in this thesis.

1.1.1 Current state of integrated optical biochips

In earlier research at our lab, a UV laser was used to write microchannel walls in spun-on UV-curable Norland optical adhesives (NOAs) on a glass substrate [6]. The uncured adhesive was washed away and the channels were sealed with a thin microscope slide cover. A laser-written crossed channel system with a glass lid is shown in Figure 1-2(a). The same method was used to write optical waveguides. An intersection of laser-written channel walls and a waveguide is shown in Figure 1-2(b). The detection of scattered light from microparticles was demonstrated to prove the feasibility of this method. The advantages of this method are fast and low cost, as the total fabrication time described above is on the order of one hour. Also, there is no mask involved, which is usually used in MEMS fabrications, and the design of microchannels and waveguides is realized flexibly by controlling the movements of the substrate relative to the focused laser spot in a LabVIEW program. A drawback of this method is that the polymer structures are not very robust and cannot stand up to the rough handling that the microchannels are subjected to when connected to external fluid pumps.

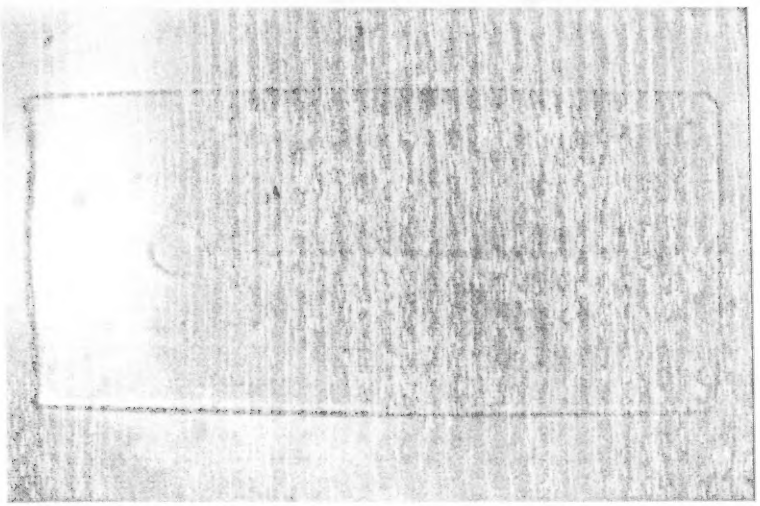

(a)

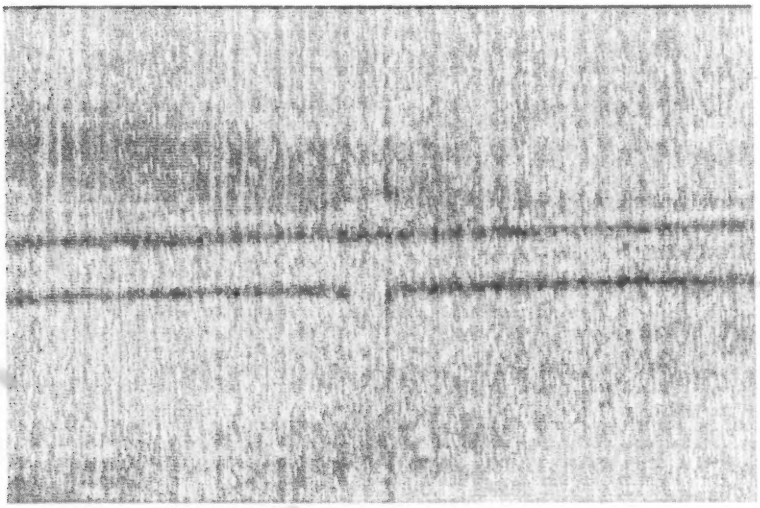

(b)

Figure 1-2 (a) Laser-written crossed channel system with a glass lid. Circle at left is a reservoir for introducing fluid samples. (b) Laser-written channel walls (horizontal) and an intersecting waveguide (vertical), the channel walls are in 100-200μm scale.

In the Harrison lab in the Department of Chemistry at the University of Alberta, a thermal ion-exchange technique was used to fabricate waveguides on glass substrates and microchannels were etched on the same substrate [8]. Fluorescence tests were performed by injecting dyed fluids into the microchannels, but the waveguide losses proved too large for the performance to be evaluated.

In other research, a group in Denmark formed etched microchannels on a Si substrate and waveguides on a doped silicon dioxide (SiO_2) layer on the Si substrate [9]. Laser light was launched into a microchannel through a waveguide and the fluorescence from a fluorescent solution was inspected. However, a difficulty in using Si for biochip fabrications is that conductive Si cannot be used for electrophoresis or electroosmosis where high electric fields are required for driving and dividing samples.

PDMS is a promising polymer material for biochip fabrication. Many researchers around the world (including our lab) are interested in fabricating microchannels using PDMS since it is stronger than normal polymers, and the processes involved are inexpensive and simple. Considering the transparent nature of PDMS, it may be a candidate material to fabricate waveguides. It is seen as a new research area for fabricating integrated optical biochips in our lab.

1.2 Overall research theme

Figure 1-3 describes the basic research theme of our lab on three scales.

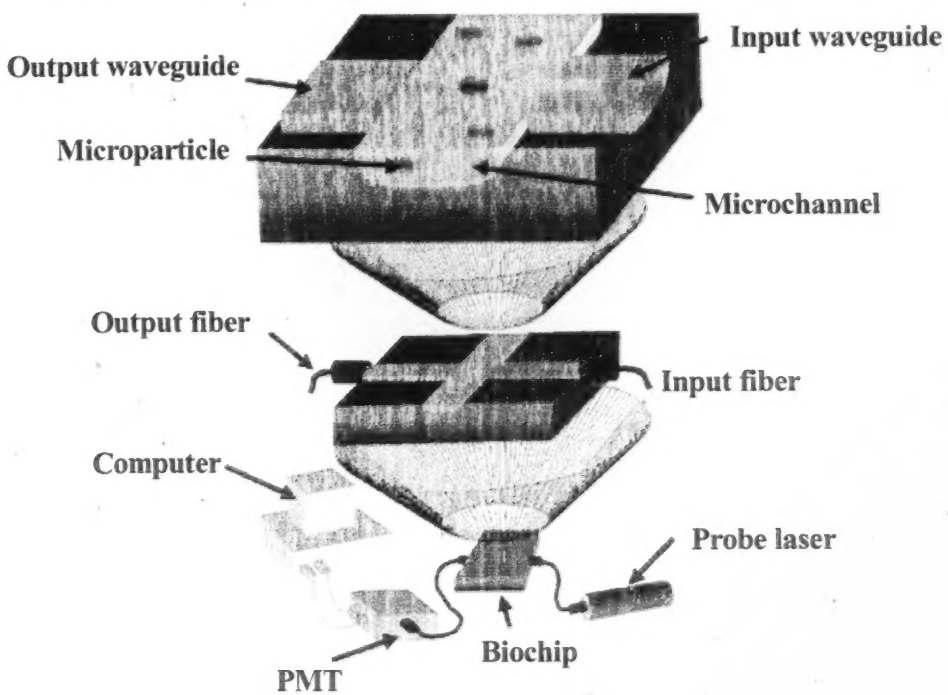

Figure 1-3 A view on three scales of the research at our lab.

At the microscopic level, microparticles (for example, blood cells or bacteria) move in a microchannel that intersects with an optical waveguide delivering incident light into the microchannel. Fluorescence from the excited microparticles is picked up by the output waveguide. The center part of the figure shows how the waveguides may be connected to the outside world with optical fibers. The lower level shows the macroscopic system with the external light source, detector (PMT) and data acquisition system (computer).

1.2.1 PMT detection system

A photomultiplier tube (PMT) detection system, assembled in earlier research at our lab [10] is used detect microparticle fluorescence signals as small as picowatts and a set of LabVIEW programs were written to control the PMT and collect the output. A PMT is a versatile device that provides extremely high sensitivity and ultra-fast response. It generates a cathode current when photons strike on the photocathode of the PMT, and multiplies the number of the electrons when they hit a cascade of dynodes. The result is a high output pulse in the form of an anode current. The ratio of the anode current to the cathode current is known as the gain of the PMT, and can easily reach 10^7. The gain mainly depends on the voltage that is applied to the PMT.

The PMT (Hamamatsu R2949) and high-voltage socket (Hamamatsu C6271) are contained in a light-proof metal box as shown in Figure 1-4. The light to be measured enters the PMT pick-up fiber, which is plugged into an optical assembly containing a ball lens and two narrow bandpass filters. The filter bandpass is centered at the fluorescence peak of the microparticles (FluoSpheres polysterene microspheres from Molecular Probes, with a diameter of 15.5 μm and scarlet fluorescence at 700 nm) and suppresses other background light. The ball lens collimates the light from the pick-up fiber and increases the throughput of the signal. The high voltage (and therefore the gain) of the PMT is controlled by an external 0-5V source supplied from a National Instruments data acquisition (DAQ) Board controlled by LabVIEW programs. Internally, the PMT socket converts 0-5 V voltage into the range of 0–1250 V. The current-to-voltage

converter on the other hand provides an output voltage, which is exported into computer through the DAQ board in a range of 0-10 V.

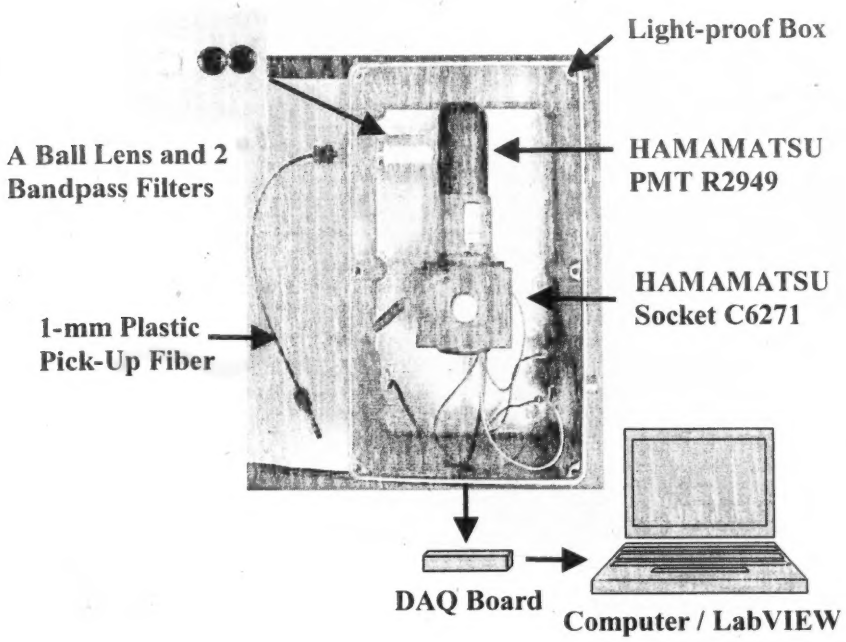

Figure 1-4 PMT setup and computer control system

The PMT detection system was calibrated to measure light in the range of gains of 10^4 to 10^7. For example, for a gain of 10^7, the nearly linear relation of the PMT output voltage y in mV and the light input power x in nW has been determined empirically, as shown in Equation (1). The other gains fall in similar equations.

$$y = x^{0.998} * 7430.19 \qquad (1)$$

1.2.2 Microparticle detection in biochips

In our microfluidics experiments, microparticle transportation and manipulation in microchannels were practiced on Micralyne biochips by using the capillary attraction, injecting fluids with a syringe and applying eletroosmosis in the microchannels. Detection of microparticle fluorescence was demonstrated by injecting a microparticle solution into micralyne biochips and FISHERbrand glass micropipettes, or simply dropping the solution onto microscope slides. The

microparticle solution at different concentrations was made from mixing de-ionized (DI) water with FluoSpheres microspheres.

A simplified scheme of an often-used fluorescence detection setup in our lab is shown in Figure 1-5. He-Ne laser light at 633 nm shines on a microchannel containing microparticles from the side. Fluorescence from microparticles is picked up by the PMT detection system. The amount of the fluorescence signal captured by PMT varies with the incident light power, the microparticle positions in the microchannel, the amount of dye permeated in microparticles, and the time length that microparticles are exposed to the laser light because dye photo-bleaches with the exposure time. One disadvantage of this setup is that both the laser light and the PMT pick-up fiber need to be aligned with microparticles. This is difficult to achieve especially when an absolute control of microparticle has not been achieved. Also, the incident light may enter the PMT pick-up fiber directly and add to the background signal, although the bandpass filters of the PMT system suppress most of it.

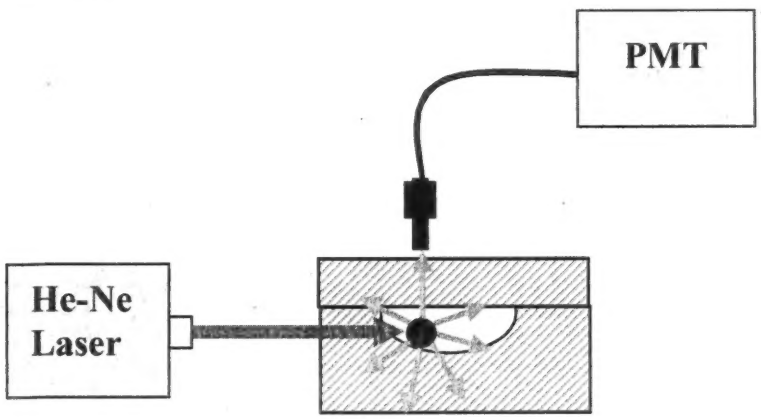

Figure 1-5 Simplified scheme of the microparticle fluorescence detection setup.

A launch-and-detect (LAD) detector was invented to solve this problem. Two 1-mm plastic optical fibers were ground and polished at the side at an approximately 10^{o} angle, until one half of the core remained at the end of each fiber. The remaining fibers were positioned side by side with polished surfaces in contact and inserted into a conical plastic syringe tip to hold them together, as

shown in Figure 1-6(a). Then the ends of the fibers were trimmed and polished. Laser light is delivered to the biochip through the launch fiber, and a portion of the fluorescence from a microparticle automatically enters the detect fiber beside the launch fiber. The setup and operation are greatly simplified by moving the launch and detect fibers together as a unit. Also, by this arrangement, though the biochip still reflects some laser light into the detect fiber, the laser light that directly enters the PMT is small, so that the background noise is reduced.

Figure 1-6(b) shows a top view of the LAD detector under a microparticle in a microchannel. The input light was dimmed to enable the taking of the picture. The 3-dimensional spatial responses of the LAD detector were measured by moving a stable microparticle in a microchannel in a 10x10 horizontal grid at the detector surface and also by moving away from the detector. The maximum response appeared where the microparticle was in the center of the detector surface and the biochip was as close as possible to the detector. The LAD detector and its lateral spatial response were later used to measure microparticle velocities in a flowing medium in another experiment conducted in our lab [11].

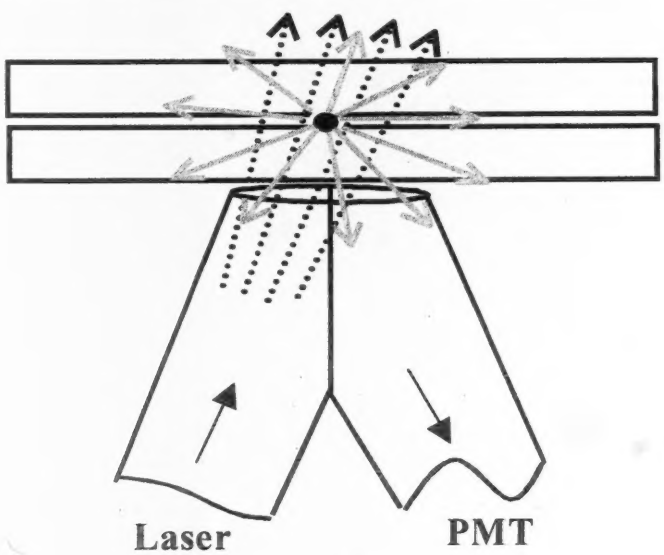

(a)

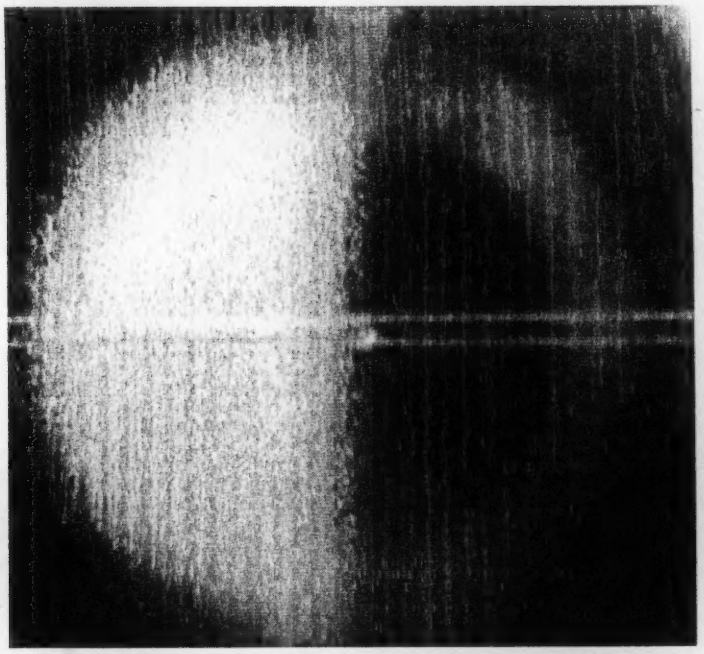

(b)

Figure 1-6 (a) Microparticle detection with an innovated launch-and-detect (LAD) detector. (b) Top view of the LAD detector under a microparticle in a microchannel. The microparticale is at the center boundary of the two fibers.

However, at this time, the techniques of manipulating microparticles to required positions in microchannels have not been developed in our lab. Therefore, we are not going to demonstrate microparticle detection in this thesis. Instead, fluorescence detection was conducted by injecting a dye solution into the microchannels we fabricated.

1.3 Outline of this research

The major goal of this project is to develop an integrated optical biochip with ion-exchange waveguides as the optical system and etched microchannels as the fluidic system on a glass substrate. The advantages of such an integrated biochip are: glass-etched microchannels are robust for handling; glass is low conductive so that electroosmosis and electrophoresis can be applied in microchannels for some microfluidics applications; glass waveguides are compatible with optical fibers, have potentially low propagation losses and

immunity to optical damage. To achieve this goal, fabrication methods, process problems, and performance evaluations have to be addressed for microchannels, waveguides, and their integration on a biochip respectively.

Chapter 2 presents a glass wet etching method to fabricate the traditional biochip similar to Figure 1-1 in the Micromachining and Nanofabrication Facility (NanoFab) in the University of Alberta, followed by a discussion about the processing issues in the fabrication.

Chapter 3 summarizes the ion-exchange mechanisms and fabrication methods used to create optical waveguides on glass substrates. This includes a brief description of the dry film field-assisted ion-exchange process developed earlier in our lab. After a few critical process problems are discussed, the relations of the ion-exchange parameters, the resulting ion-exchange currents and waveguide depths, and the evaluation of the waveguide profiles and waveguide properties (including waveguide losses) are presented.

Chapter 4 addresses the problem of integrating microchannels and waveguides on a single chip. Two possibilities are described in detail. It was determined that the preferred procedure was to fabricate waveguides in the glass substrate first, then etch the microchannels. The delivery of light to the microchannels is demonstrated by detecting fluorescence signals from a dyed fluid in the microchannels.

Finally, Chapter 5 summarizes the results achieved and offers suggestions for future work.

2 FABRICATION OF TRADITIONAL BIOCHIPS

2.1 Introduction

A wet chemical etching method involving Hydrofluoric acid (HF) is typically used to fabricate microchannels in glass substrates. Figure 2-1 shows the cross-section of the Micralyne biochip in Figure 1-1. Isotropic wet etching generates a semicircle-like cross-section of microchannels in the glass substrate. In the same process, 1-mm-diameter reservoirs are etched at the ends of the microchannels to contain studied fluid. A cover plate with 2-mm-diameter via holes, through which the reservoirs are able to connect to external fluid sources, is then fused onto the substrate to enclose the microchannels.

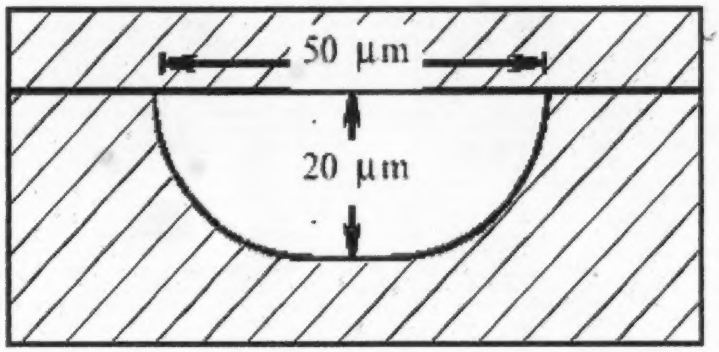

Figure 2-1 Approximate cross-section of a Micalyne biochip.

In this project, we etched microchannels on ten Corning 0211 substrates and one Schott Borofloat substrate, seven of which were bonded to cover plates drilled with via holes. Glass etchants contain hydrofluoric acid (HF), one of the most dangerous chemicals in the NanoFab. Extra protective clothing is required, and strict safety procedures must be followed.

2.2 Process summary of fabricating microchannels

The fabrication was carried out in the NanoFab and at Micralyne Inc. Refer to Appendix 1 for more details of the process steps described briefly below.

1. Sputter 20-30 nm thick Cr and 200-300 nm Au on a clean substrate.

2. Spin on HPR 504 photoresist, hard bake, and expose.

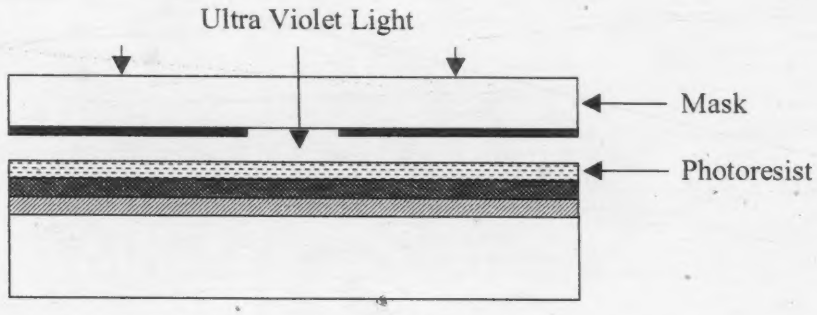

3. Develop photoresist, etch Au and Cr.

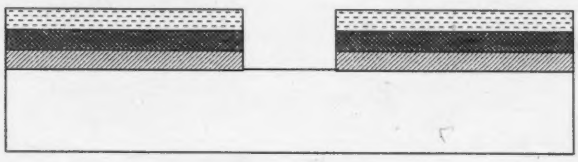

4. Etch glass to form microchannels. Protect the backside of the substrate from being etched with a piece of black tape.

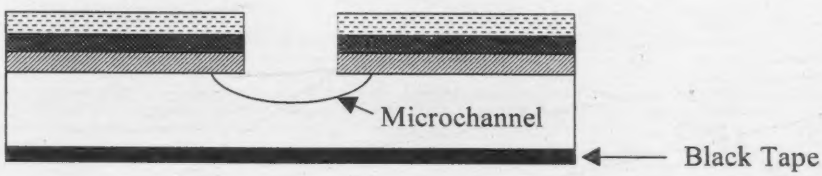

5. Remove photoresist and metals from the surface. The bottom substrate with the microchannels is ready for bonding.

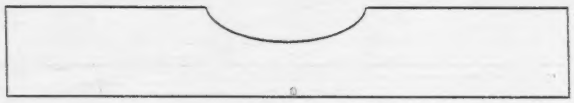

6. Drill via holes in a cover plate. Protect the cover plate with two pieces of protective glass glued with Crystalbond™, and drill via holes through the cover plate.

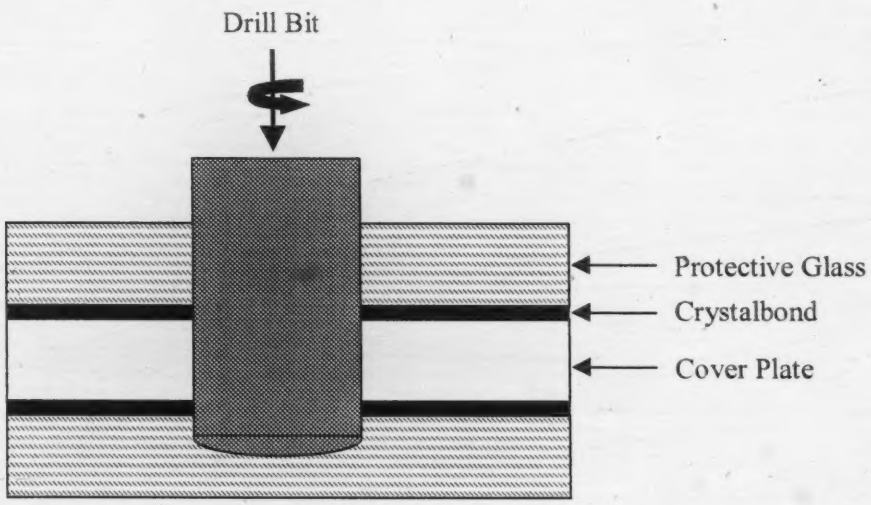

7. Bond the cover plate with the bottom substrate. Clean both of them rigorously, align via holes with the reservoirs, bond and bake the substrates in 300°C for 3 hours. Cut and polish the bonded biochip.

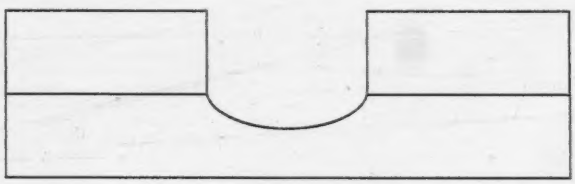

2.3 Processing issues

Three major processing issues became apparent during the development of the biochip fabrication steps.

2.3.1 Glass metallization

In the NanoFab, we sputter 30 nm Cr and 190 nm Au on clean glass, and later spin 1 μm HPR 504 photoresist to generate the channel pattern and also to protect the glass. The etching result in

Figure 2-2(a) shows that, the metals at the mask openings often lift off during the glass etching. Consequently, the substrate underneath loses its protection and is etched by the glass etchant as well. We also find that some spike-shaped etchings occur in the channel walls where the metals are not lifted, as shown in Figure 2-2(b). These are commonly reported problems for microchannels made in the NanoFab. Metals often do not adhere well to a smooth and clean glass surface. Therefore, any contamination from the cleaning process or the sputter chamber is a potential source to initiate metal lifting from the area around the contamination.

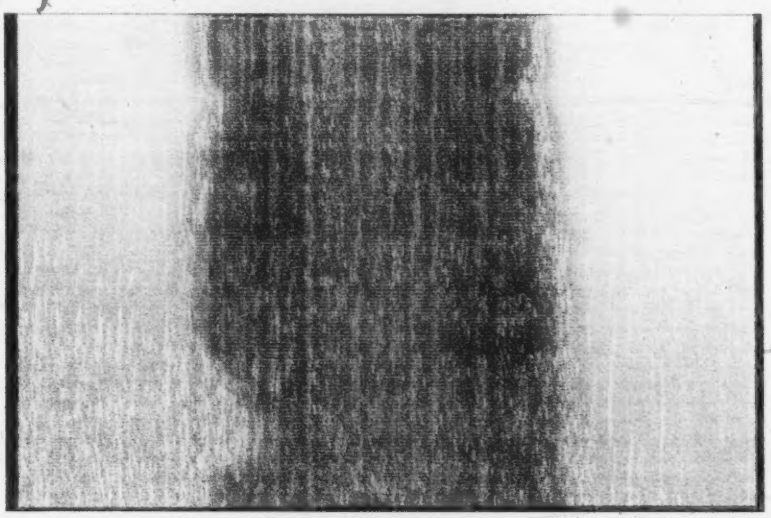

(a)

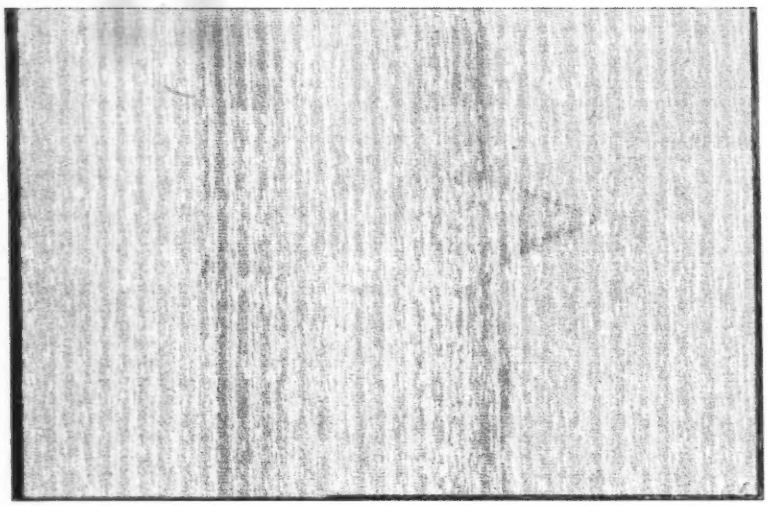

(b)

Figure 2-2 Microchannels etched in the NanoFab. (a) Mask lifting around a 10 μm channnel during glass etching. (b) Spikes-shape etching on the channel walls.

To solve this problem, one sample was taken to Micralyne, where an extra step, radio frequency (RF) etching, was used before sputtering Cr. RF etching roughens the glass surface by removing a few nanometers glass material. As a result, sputtered metal atoms adhere better to the porous glass surface. Then, 20 nm Cr and 230 nm Au were sputtered on the substrate in Micralyne. After the sample was taken back to the NanoFab, HPR 504 photoresist was spun on and the substrate was etched using the same glass etchant as the other samples. The etching result was inspected using a microscope, and no metal lifting or spikes were found on this sample. This proves the efficacy of RF etching to improve the metallization process.

2.3.2 Bonding and cleaning

The bonding of the cover plate and substrate with microchannels occurs in two steps: initial bonding and post bake. Initial bonding refers to a cold welded bond achieved when two pieces of clean glass have an intimate contact at room temperature. An initial bonding can keep two pieces of glass together temporarily until they are separated by, for example, inserting a sharp blade between the glasses. However, for the microfluidics applications, biochips are subjected to

routine handling and applied pressures, such as injection of fluid. A post bake at an elevated temperature is often applied to form a permanent bond of substrates.

Initial bonding is mainly determined by the cleanliness and flatness of glass. Ref. [12] describes a very sophisticated cleaning and bonding process at room temperature used by Harrison's group in the Department of Chemistry at the University of Alberta. In our experiments, a hot piranha bath and diligent scrubbing of the bonding surfaces with a sponge were used to remove metal residue, crystalbond^{TM} residue, and stubborn particles, followed by a sufficient dump rinsing and blow dried with a N_2 gun from certain angels (details in Appendix 1). If Newton rings occurred on the bonded interface during the initial bonding, the bonded substrates had to be taken apart under water and the cleaning was repeated starting from scrubbing the bonding surfaces. By the cleaning steps above, initial bonding was achieved on Corning 0211 and Schott borofloat glass respectively, and bonding results were improved by a post bake followed. However, for glass that does not have an initial bonding, post bake can not fuse the glass together. We conducted the same experiment on FISHERbrand® microscope slides, which had no initial bonding after a rigorous cleaning. After a post bake at 350°C for 5 hours with weight pressing the slides together, the slides were still separated.

2.3.3 Microchannel etching results

Figure 2-3 shows a SEM image of a 28-μm-deep 86-μm-wide microchannel we made with a 11-μm-wide opening on the quartz mask.

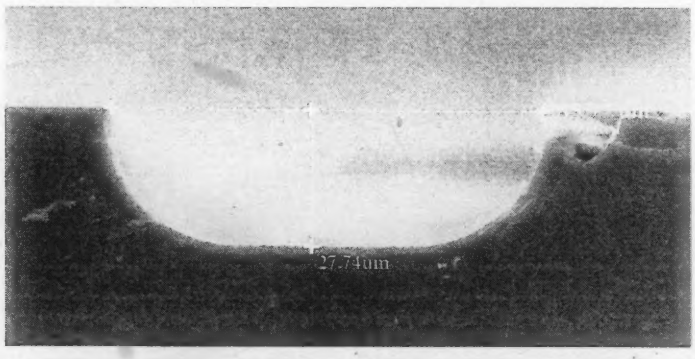

Figure 2-3 SEM image of a cross-section of a 28-μm-deep 86-μm-wide microchannel.

Theoretically, the isotropic wet etching leads to an undercutting which results in a microchannel width equal to twice that of the microchannel depth, plus the mask opening. From this calculation, a 28-μm-deep microchannel should have a width of 67 μm. However, when the substrate stays in the glass etchant for a long time, usually 30 min to 1 hour to etch a 30-μm-deep microchannel, the photoresist and metal protections are also gradually eroded by the etchant, as illustrated in Figure 2-4. The lateral expanding of the mask opening results in an extra width increase of nearly 20 μm in the microchannel when a 28-μm depth is etched. In future microchannel fabrications, smaller mask openings should be designed on the microchannel mask to compensate for this effect.

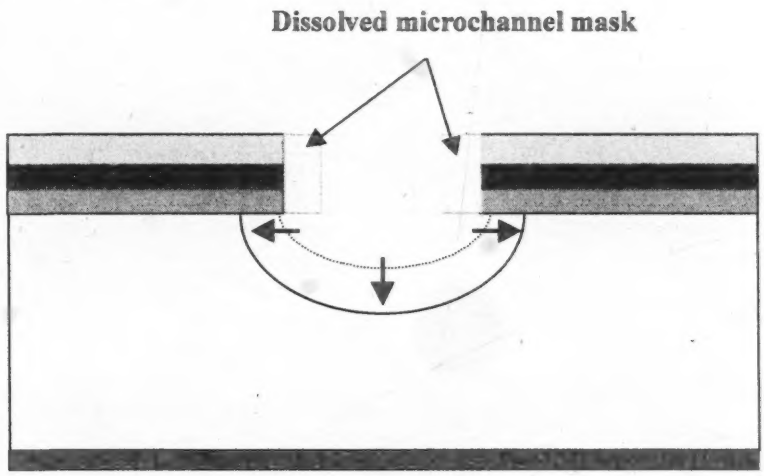

Figure 2-4 Undercutting of the isotropic glass etching and lateral expanding of the microchannel mask opening.

3 FABRICATION AND CHARACTERIZATION OF ION-EXCHANGE WAVEGUIDES

3.1 Introduction

Ion exchange has been used for more than a century to produce tinted glass. Relations of various parameters involved in the exchange and diffusion of alkali ions in glass have been extensively studied in Ref. [13]. In 1972, Izawa and Nakagome [14] first reported that the ion-exchange process could be utilized to produce waveguides because a refractive index change happens with any alteration of the electronic structure of glass.

3.1.1 Ion-exchange mechanisms

Sodium ions, present in common glasses such as soda limes and borosilicates, are known for their high mobility and therefore exchange well with monovalent alkali ions. The refractive index can be increased or decreased as a result of a combination of the following three major physical changes of glass: (a) the ionic size of the exchanging ions, (b) the electronic polarizability of the exchanging ions, and (c) the stress induced by variation of glass volume. Table 3-1 lists relevant ion-exchange parameters for a number of common alkali ions.

Ion	Li^+	Na^+	Ag^+	K^+	Rb^+	Tl^+	Cs^+
Ionic Radius (Å)	0.65	0.95	1.26	1.33	1.49	1.49	1.65
Electronic Polarizability ($Å^3$)	0.03	0.41	2.4	1.33	1.98	5.2	3.34

Table 3-1 Relevant ion-exchange parameters of common alkali ions.

(a) The ionic size of the exchanging ions

If a smaller ion such as Li^+ replaces a larger ion such as Na^+ or K^+, the glass network will collapse around the smaller ion to produce a more densely packed structure that usually has a higher refractive index. Conversely, if a

larger ion replaces a smaller ion, the network expands to a less packed structure, yielding a lower refractive index.

(b) The electronic polarizability of the exchanging ions

If an ion of larger electronic polarizability such as Tl^+, Cs^+, Ag^+, Rb^+, or K^+ replaces an ion of smaller polarizability such as Na^+, an increase in the refractive index will result, and vice versa. The increase in the refractive index as a function of the electronic polarizability can be shown to be [15]

$$\Delta n = \frac{(n^2+2)^2}{6n}\frac{4\pi}{3V}\sum_i \Delta Q_i \alpha_i \qquad (2)$$

where n is the refractive index of glass, V is volume of glass, ΔQ_i is the number of type (i) ions replaced, and α_i is their electronic polarizability. In addition, secondary effects such as the electronic polarizability of the neighboring (oxygen) ions may have to be also considered in order to justify the index change obtained experimentally.

(c) Stress

Stress is generated because of the different ionic radii of the exchanging ions and the different thermal expansion between the exchanged glass region and the substrate. The stress profile generally follows the concentration profile of the incoming cations. The lateral component of stress is normally much bigger than the vertical component, because glass can expend or contract at the surface to form swellings or dips. Besides mechanical effects, such as swellings or dips, and microcracks on the surface, the main optical effect of stress is that the two polarizations, TE and TM, have different refractive indices due to their different connection with the stress components [16]. The resulting waveguides are birefringent. By adjusting the ion-exchange parameters, stress and its effects can be reduced.

3.1.2 Fabrication methods

Traditionally, ion-exchange waveguides were fabricated using molten salt baths to replace alkaline ions in the glass, e.g. KNO_3, $TlNO_3$ or $AgNO_3$ to replace

Na^+, and $CsNO_3$+CsCl to replace K^+. A schematic diagram of ion exchange in an $AgNO_3$ bath is shown in Figure 3-1(a). In a molten salt bath, the exchange of ions occurs by pure thermal diffusion. Silver ions are driven by an interphase chemical potential gradient, and Na^+ ions are released into the bath in order to maintain charge neutrality. The process usually takes several hours to diffuse the ions under the surface to make single and multimode channel waveguides.

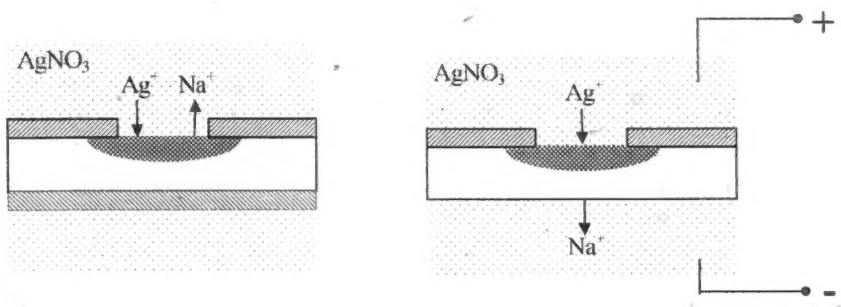

(a) (b)

Figure 3-1 (a) Schematic diagram of ion exchange in a $AgNO_3$ bath. (b) Thermal diffusion is accelerated with an electric field applied in $AgNO_3$ baths.

However, this process can be accelerated by applying an electric field across the glass sample with the aid of immersed metal electrodes in the top and bottom salt baths [14], as shown in Figure 3-1 (b). The applied electric field assists in driving Ag^+ ions more rapidly towards the negative electrode and causes the ions to drift deep into the glass. Sodium ions are driven out of the glass into the bottom bath from the backside of the glass. A variation of this setup is to use a metal film cathode instead of the bottom bath [17]. In this case, a layer of Na metal is accumulated between the glass surface and the metal cathode.

An alternative approach to make ion-exchange waveguides is to use a solid metal film on the surface of the glass as the ion source, first presented by Chartier et al. in 1978 [18]. Among the various alkali ion sources, this technique is by far mostly used for Ag ion exchange since Ag films can be easily deposited and maintained in a stable form. As shown in Figure 3-2(a), a Ag film is deposited on a structured mask as the ion source, and a metal layer is deposited on the backside

of the glass to ensure the electric contact. Ion exchange is carried out at an elevated temperature with the aid of an electric field applied across the sample. Under this condition, Ag^+ ions can be released by an electrochemical reaction in which the metal is oxidized as the follow [19]:

$$Ag \rightarrow Ag^+ + e^-$$

Silver ions are driven into glass by the applied drift field $\vec{E}$ with a distribution in Figure 3-2(b), which is numerically solved with a nonzero flux distribution, surface boundary conditions, and glass nonhomogeneous electrical conductivities [17]. Sodium ions are driven out of glass from the backside and a layer of Na metal is accumulated between the glass surface and the metal cathode. A variation of this setup is to use a molten salt bath as the cathode to avoid deterioration of the glass backside by Na accumulation [20].

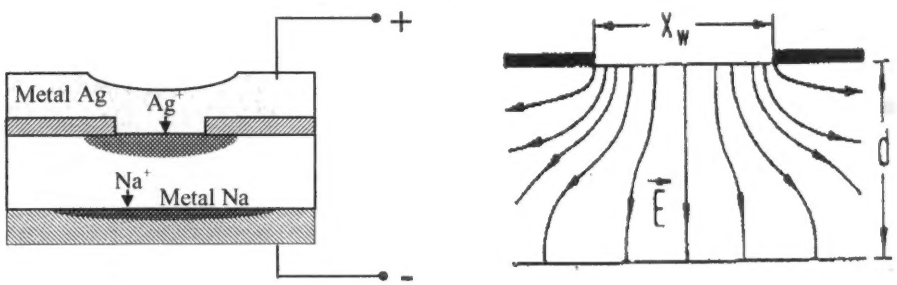

(a) (b)

Figure 3-2 (a) Schematic diagram of dry film field-assisted ion exchange. (b) Electric field in glass sovled in [17] for dry film field-assisted ion exchange.

It should be noted that in the absence of an applied voltage, only a small Ag concentration inside the glass surface is found. Ref. [21] reported no significant ion exchange occurred after processing for 7 hours at 283°C. At 275°C, an applied electric field as small as 1 V/mm [20] can cause the Ag ions to overcome the electrochemical potential between the Ag film and the glass substrate. However, it is suspected that the temperatures used above are too low to energize many Ag^+ ions to overcome the boundary energy without an applied field. There is no further

result reported at higher temperatures in the absence of an applied voltage. It is not clear whether the field assistance is essential for dry film ion exchange.

In our research, we need to fabricate 20-30 μm deep waveguides, which are of similar depth as the microchannels, and also compatible to the optical fiber. We decided to use the dry film ion-exchange technique to fabricate waveguides because it has been more extensively studied in recent research than the molten bath technique due to the following distinct advantages:

1. It eliminates the need to use a special setup to hold the molten salt and substrates. The process is relatively clean as pure silver film is deposited on a clean substrate and the ion exchange is carried out in a closed atmosphere.
2. The total amount of the Ag^+ ions in the glass can easily and accurately be controlled by the ion exchange time and the current density, or alternatively, by the silver film thickness. Also, the refractive index profiles of the waveguides are very insensitive to temperature variations during the fabrication and the surface index of the waveguides can be controlled in a wide range.

3.1.3 Substrate selection

A large variety of glass substrates are used in ion-exchange research, including ordinary microscope slides, soda lime, Corning borosilicate, BK7, BF450 [22], Schott TiF_6 [23], and Schott borofloat glass substrates. Many factors in glass substrates such as composition, Na concentration, and ionic radii variation [23] affect self-diffusion coefficients of exchanging ions. Also, some glasses contain electron donors, like As_2O_3, Sb_2O_3, or FeO, which are responsible for the reduction of Ag^+ ions to Ag atoms as a result of the following reactions [15].

$$Ag_2O + 2FeO \rightarrow Fe_2O_3 + 2Ag$$

$$2Ag_2O + As_2O_3 \rightarrow As_2O_5 + 4Ag$$

The submicroscopic crystals of Ag are believed the main reason of the scattering loss of ion exchange waveguides. Corning 0211 glass and Schott borofloat glass are two types of borosilicate glass commonly used in the

applications of biochips for DNA analysis. In our lab, Corning 0211 glass was used earlier as the substrates for fabrication of polymer waveguides and microlenses, and developing the ion-exchange process. The Micralyne biochips on which we are experimenting with microfluidics are fabricated from Schott borofloat glass. One of the most attractive advantages of borosilicate glass is that the ratio of the self-diffusion coefficients, $M= D_{Ag}/D_{Na}$, is about 0.7 [24], while it is only 0.1 in common sodium silicate glass. As a result, borosilicate glass has more uniform glass conductivity and a smaller sodium depletion region than sodium silicate glass. Also, no As_2O_3, Sb_2O_3, or FeO are shown in the composition sheets of Corning 0211 and Schott borofloat glass.

In earlier research of our lab [25], the dry film ion-exchange process was introduced to the NanoFab in the University of Alberta, and a variety of experiments with different metal layer combinations (mask layer, cover layer and cathode layer) were conducted. The optimum material combination Au/Ag/Cr/Glass/Ag (from front to back) was suggested to fabricate channel waveguides. In this research, we demonstrated the ion-exchange process on 31 Corning 0211 and 4 Schott Borofloat substrates, on three of which channel waveguides were fabricated successfully. A few important issues were discovered in the process and problems were resolved to enable the process and improve the waveguide qualities.

3.2 Fabrication of ion-exchange waveguides

Most of the waveguide processing was carried out in the NanoFab in the University of Alberta with the assistance of NanoFab staff. Refer to Appendix 2 for more details of the process steps described briefly below.

1. Sputter 500-nm-thick Cr on a clean substrate.

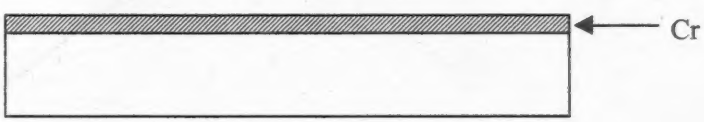

2. Spin on HPR 504 photoresist, hard bake, and expose.

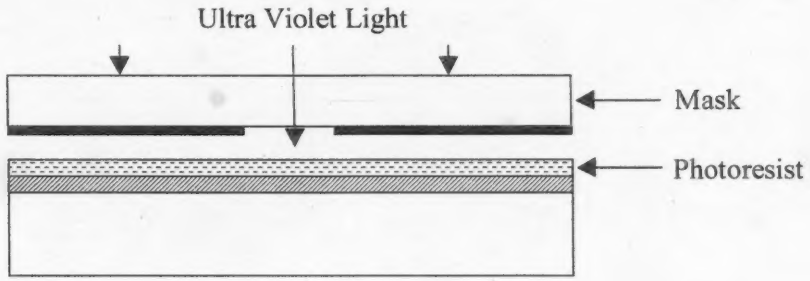

3. Develop photoresist, and etch Cr.

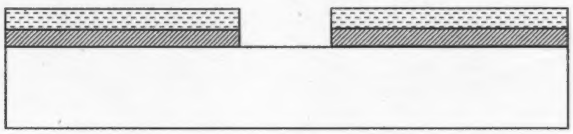

4. Remove photoresist, and oxidize Cr in a furnace.

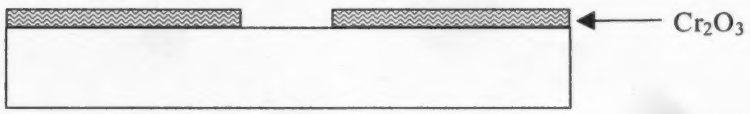

5. Sputter 1.5-μm-thick Ag on both sides of the substrate, and 1-μm-thick Au on the front side as a cover layer to protect Ag and also ensure electric conductivity.

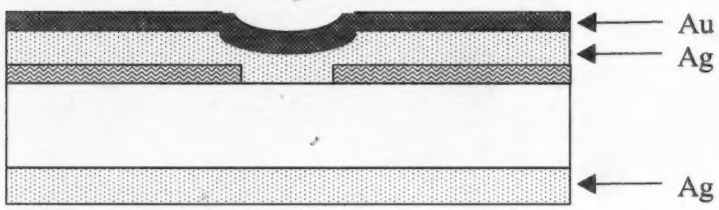

6. Drive Ag^+ ions into the substrate at an elevated temperature (280 to 400°C) and an applied electric field (35V/mm to 285V/mm) to form ion-exchange waveguides.

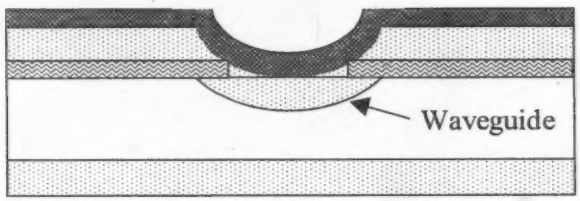

7. Remove all the metals from the surface, dice and polish the substrate for waveguide property tests.

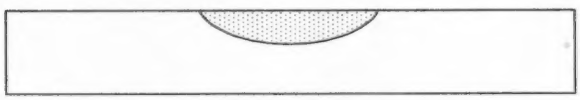

3.3 Processing issues in waveguide fabrication

Several issues arose during the development of the waveguide fabrication process. These problems and their solutions are described below.

3.3.1 Ion-exchange mask

In the literature, Cr has often been cited as the mask material for fabricating ion-exchange waveguides. However, the waveguides we made with a Cr mask all have structures similar to Figure 3-3. Apparently, silver ions broke thorough the Cr film and migrated into the substrate. With the existence of the Cr film, the waveguide depth was slightly smaller than those below the mask openings.

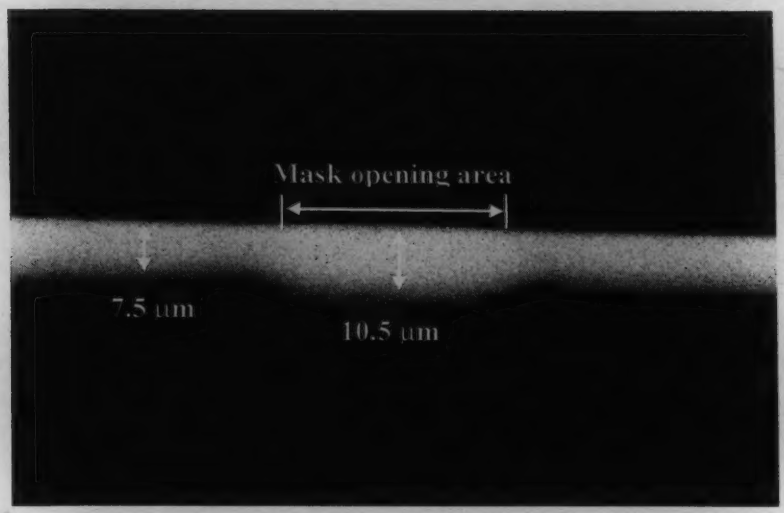

Figure 3-3 SEM iamge of waveguides using a Cr mask.

To prevent the Ag from migrating through the Cr film, we tried to adjust many experiment parameters, including using a lower temperature, smaller electric field and thicker Cr film, and testing on different substrates, but without improvement. Along with this problem, bubbles were formed along the mask openings under the Ag film, as a result of decomposition of photoresist residue at ion-exchange temperatures. To completely remove the photoresist, in addition to the photoresist removal process, a substrate was heated in a furnace at 380-400°C just before sputtering Ag. At this temperature, the photoresist was burned off and Cr was oxidized to Cr_2O_3 in the air environment. This is indicated by a change in film color. The SEM result shows that Ag^+ ions are only driven in to the substrate in the mask opening area on this substrate. Thus, Cr_2O_3 works well as the ion-exchange mask.

We believe the reason Cr_2O_3 is a better ion-exchange mask is as follows. The Cr film sputtered using the parameters recommended in the NanoFab is not very dense. Ag^+ ions may migrate through the spaces between Cr atom clusters when they are driven by the electric field. When Cr is oxidized in the furnace, oxygen ions fill in the spaces and densify the film, so Cr_2O_3 film is able to block the Ag^+ ions. For the same reason, photoresist has good adhesion to a coarse Cr film, so that the photoresist removal process is not adequate to remove the

photoresist completely. We did not examine the Cr and Cr_2O_3 films experimentally. However, to achieve a dense Cr film, sputtering parameters need to be adjusted, and a better chamber vacuum, meaning longer pump down time, is required.

With this extra heating step, another interesting phenomenon occurs to two identical Corning 0211 substrates that are carried though the same processes. After heating in the furnace, the mask edges on both substrates were raised up approximately 150 nm, as shown in the Figure 3-4(a). One substrate was taken to sputter Ag and conduct ion exchange with raised mask edges. The waveguides made on this substrate have very rough edges, as shown in Figure 3-4(b). Another substrate was treated with an additional cool piranha bath to smooth the mask edges (Figure 3-4(c)). The waveguides made on this substrate show very smooth edges in Figure 3-4(d). This process was applied to Schott borafloat substrates, resulting in similar results.

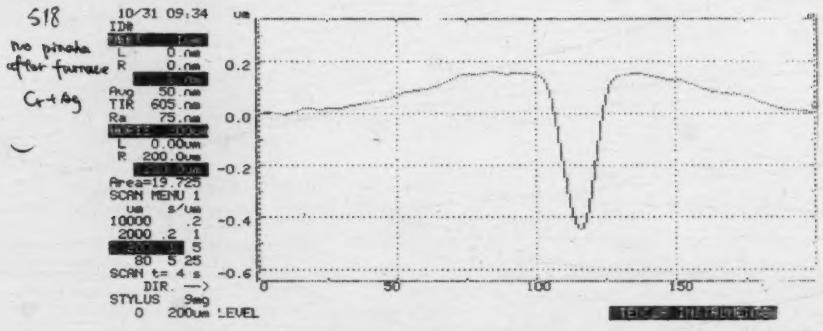

(a)

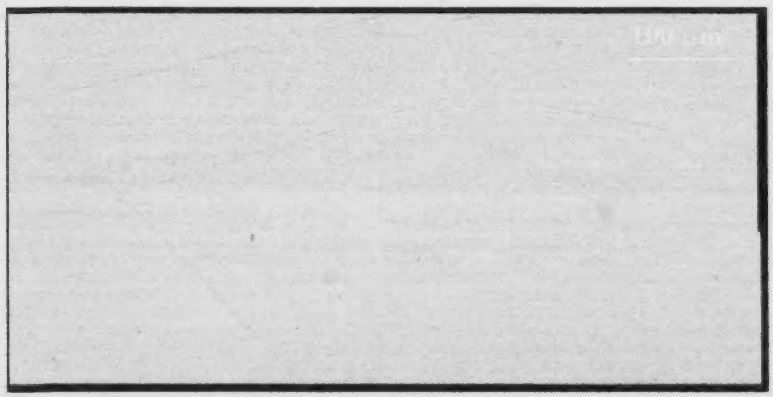

(b)

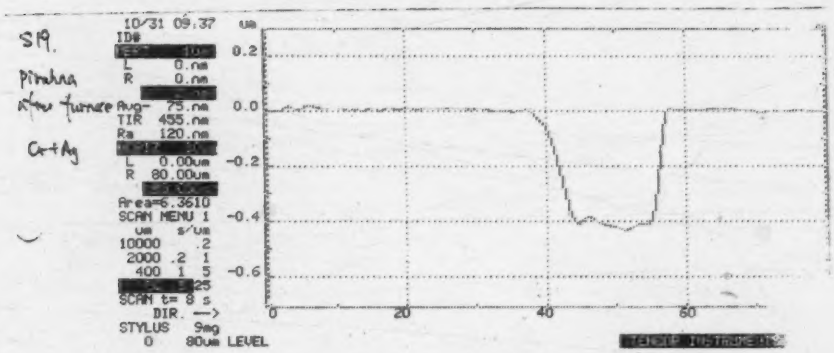

(c)

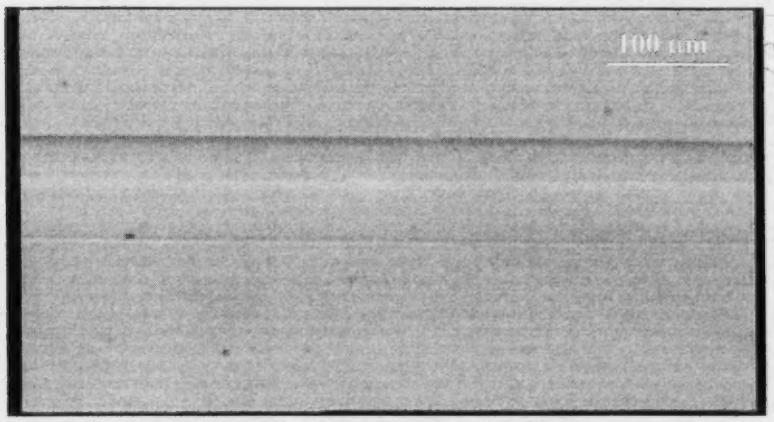

(d)

Figure 3-4 (a) Profilometer plot of a 20 μm mask opening after heating in a furnace. (b) Rough waveguide made with the mask opening with the profile in Figure 3-4(a). (c) Profilometer plot of a 20 μm mask opening smoothed by an additional cool piranha bath after heating in a furnace. (d) Smooth waveguide made with the mask opening with the profile in Figure 3-4(c).

3.3.2 Waveguide coloration

Waveguide coloration is believed to be a result of Ag^+ ions changed back into atoms in the ion-exchange process. It appears yellow because Ag atoms absorb blue light. Among two Corning 0211 and one Borofloat substrate on which waveguides were fabricated successfully, one Corning 0211 substrate has a visibly yellow color in the waveguides. Waveguides on the other two substrates (one Corning 0211 and one Borofloat) using similar ion-exchange parameters (380-400°C, 35 V/mm, 40-54 min) do not have observable yellow color, or there are no significant Ag atoms in these waveguides to make them appear yellow.

Different opinions have been given to explain this phenomenon in the literature. When a molten bath is used for the ion-exchange process in Ref. [26], comparing to the melt, the different electrical potentials of glass and the metal mask attract Ag^+ ions under the mask edges, and change Ag^+ ions to Ag atoms using the electrons donated by the metal mask. When the metal mask is oxidized, the coloration is dramatically reduced. Waveguide coloration on Corning 0211 substrates were analyzed in Ref. [27], where it was suggested that yellow waveguides are caused by the blocking anode current because of the existence of the mask, and using Ag strips instead of a patterned mask can avoid this problem. In Ref. [20], experimental results using different ion-exchange temperatures were compared, and the conclusion was made that high ion-exchange temperatures were the reason the waveguides were colored.

In our research, we did not study this phenomenon theoretically, but empirically the yellow waveguides we fabricated were related to both the ion-exchange mask and the temperature. First, the yellow color only occurred along the mask openings, as shown in Figure 3-5. Second, to evaluate the effect of temperature, we removed the mask after ion exchange, and baked a substrate with waveguides at 600°C for 30 min with no assistance of an electric field. The area outside of the mask opening in the waveguides turned yellow as well, indicating a high temperature might be a factor of waveguide coloration.

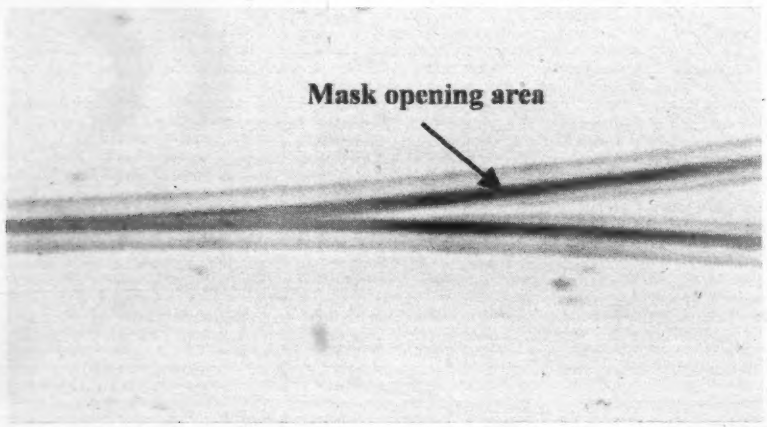

Figure 3-5 A section of a waveguide splitter. The dark lines in the center of the waeguides are the mask opening area and have visibly yellow color indicating the presence of Ag atoms.

3.4 Relations of ion-exchange parameters and results

Factors such as temperature, assisted electric field, ion-exchange time, as well as glass composition, and silver layer thickness, affect waveguide depth. We have demonstrated ion exchange over wide experimental conditions by varying different parameters including electric field, temperature, and ion-exchange time, and experimenting with different substrates, and studied the relations of currents, Ag film consumed and waveguide depths resulted.

3.4.1 Ion-exchange parameters and currents

For example, Figure 3-6 shows the current profiles for three identical substrates, with a 34.4 cm^2 diffusion area and 1.5 μm Ag on the top, using different conditions of electric field and temperature. Sample 1 was experimented with a gradually increasing temperature at a constant electric field of 136 V/mm. During the first 15 minutes after the field was turned on and the temperature was rising in the oven, the current increased nonlinearly. Between 15 minutes and 42 minutes, the current increased almost linearly as the temperature rose steadily from 330 to 355°C. Sample 2 was experimented with an electric field of 78 V/mm for approximately 1 hour at 300°C, then 1.5 hour at 350°C. The sudden rise in temperature caused a corresponding increase in the current. The ion exchange on Sample 3 was conducted at 350°C for 3 hours with an electric field of 18 V/mm, then 1.5 hours with an electric field of 76 V/mm. The rise in electric field also caused a sharp increase in the current. The silver ion source was consumed on these substrates, so all the currents show a sudden drop, which is a typical current behavior when the ion source is consumed.

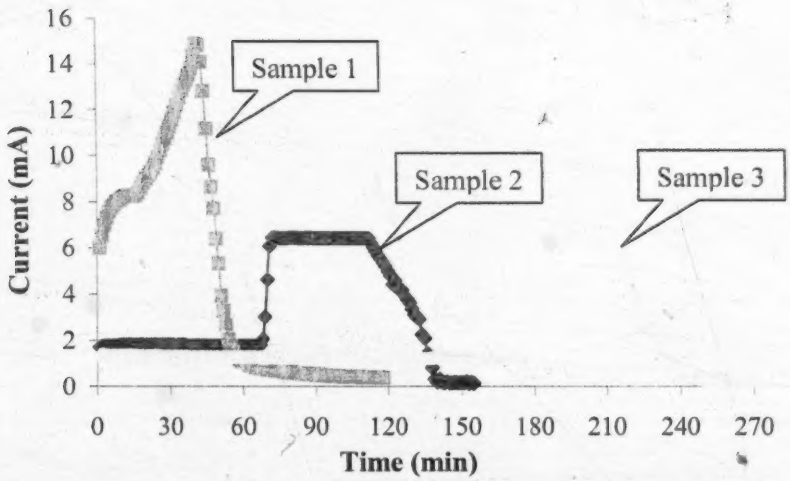

Figure 3-6 Current profiles vs. time on three identical substrates using different parameters.

According to SEM and X-ray scanning results, these substrates all generate up to 50-μm-deep waveguides and have similar Ag^+ ion concentration profiles, which agree with the results of Ref. [24] and [19]. In their theory, the waveguide depth is determined by the thickness of Ag film when it is consumed, but not by ion-exchange parameters used.

In order to measure the dependence of the current on temperature, five Corning 0211 substrates with the same diffusion area were experimented at 100 V/mm and different temperatures. Figure 3-7 shows the results and a curve fit to the data indicating the exponential nature of the dependence.

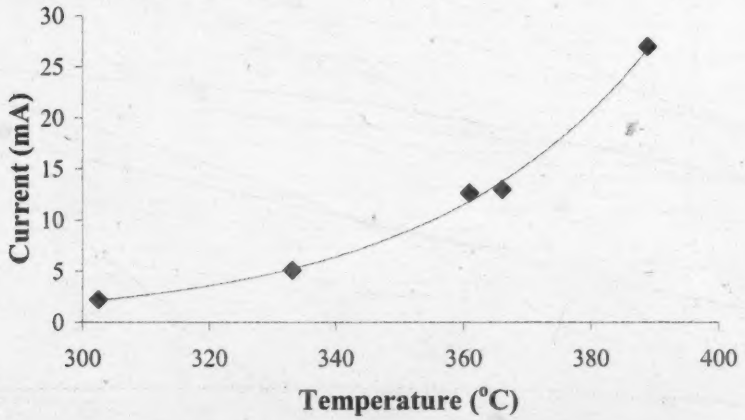

Figure 3-7 Current vs.Temperature at E=100V/mm on five Corning 0211 substrates with the same diffusion area. The data is approximated very well by an exponential curve.

We also observed that the current was linear to the electric field applied, as shown in Figure 3-8, which agreed with the result in Ref. [20] and [28]. This is easy to understand because the current fluxes at the glass surface follows [19]

$$\vec{J} = \sigma \vec{E} / F \qquad (3)$$

where σ is the conductivity of glass which is related to temperature, and F is the Faraday constant, so that the current density is proportional to the applied voltage.

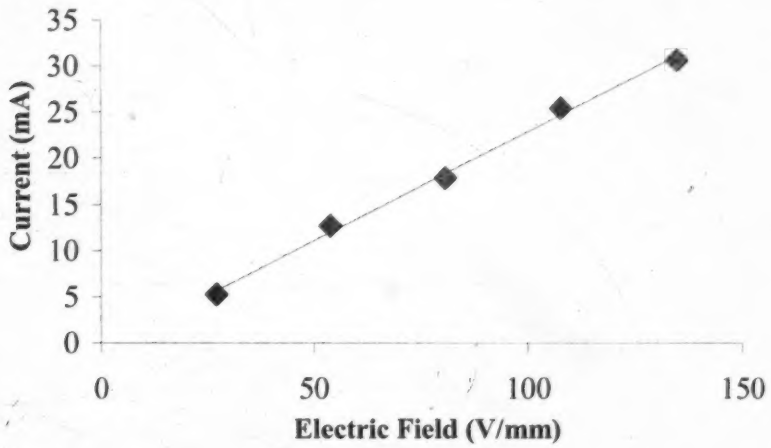

Figure 3-8 Linear relation of current with the electric field at T=360°C on five Corning 0211 substrates with the same diffusion area.

3.4.2 Currents and waveguide depths

Normally, we do not use up the Ag film so that the damaging of the substrate surface can be avoided. The ion exchange is usually stopped before a sudden drop of the current occurs. So it will be useful to find relations between the current profile, the waveguide depth and the Ag thickness consumed, which can be used to predict the depletion of ion source and estimate the waveguide depth.

The quantity of Ag for unit area is $N = d * \rho / M_{Ag}$, where d is the thickness of the Ag film, ρ is the film density, and M_{Ag} is the atomic weight of silver. Driven by an electric field $\vec{E}$=U$\vec{e}$ in Figure 3-2(b), the advancing ion front $\vec{r}$ is given by Ref. [19].

$$\vec{r} = \vec{r}_0 + \int_0^u \vec{e} / C_0 du \tag{4}$$

$$\Delta N = \int_0^u e_x du \tag{5}$$

where normalized time $u = \sigma U t / F$, σ is the conductivity of glass, U is the voltage between electrodes, t is time, F is the Faraday constant, C_0 is the original Na^+ concentration in the substrate, and e_x is the electric field normal to the glass boundary. The quantity, ΔN, of consumed Ag for unit area is proportional to the quantity of exchanged ions ΔQ through the surface with an area S as

$$\Delta N = \Delta Q / q_0 S . \tag{6}$$

By integrating the current I with time t over a total ion-exchange time T, the quantity of exchanged ions is easily obtained from Equation (7).

$$\Delta Q = \int_0^T I(t) dt \ . \tag{7}$$

Therefore, the consumed Ag thickness can be calculated in Equation (8)

$$\Delta d = \frac{M_{Ag} \Delta Q}{\rho q_0 S} \tag{8}$$

In the case of planar waveguides, Equations (4) and (5) are simplified and the waveguide depth in the substrate can be predicted to be

$$r = \Delta N / C_0 = \Delta Q / q_0 S C_0 . \tag{9}$$

We calculated the consumed Ag thickness and the waveguide depth of planar waveguides with the diffusion area S = 21cm^2 on Corning 0211 substrates using Equation (7)-(9). The ion-exchange parameters and results are shown in Table 2, where T is the temperature, V is the applied voltage, t is the ion-exchange time, ΔQ is the quantity of the exchanged ions calculated from the current profile by Equation (7), Δd is the consumed Ag ions thickness calculated from Equation (8), r_1 is the waveguide depth calculated from Equation (9), and r_2 is the waveguide depth measured from a Metricon prism coupler (Model 2010) in the TRLabs, and r_3 is the waveguide depth measured from the SEM images taken in the NanoFab. Na^+ concentration C_0, 5.7x10^{-3} mol/cm^3, can be calculated from the density of Corning 0211 substrate, 2.53 g/cm^3, and the sodium oxide (Na_2O)

weight ratio, 7%. (Other parameters used are: silver atomic weight 107.868, atomic weight unit 1.66×10^{-27} kg, silver density 10.5 g/cm^3, electronic quantity 1.6021×10^{-19} C, and the constant 6.022×10^{23} /mol.)

Sample	T (°C)	V (V)	t (min)	ΔQ (C)	Δd (μm)	r_1 (μm)	r_2 (μm)	r_3 (μm)
S6_3	366	54	120	52.1	2.6	45	41	--
S8-2	360	135	15	26.0	1.3	23	25	25
S6_4	390	54	15	24.3	1.2	21	21	--
S8-1	360	108	15	22.9	1.2	20	20	20
S7-4	360	81	15	16.1	0.8	14	14	12
S7-1	360	54	15	11.4	0.6	10	10	10
S7-2	330	54	15	4.6	0.2	4	4	2

Table 2 Ion –exchange parameters and eesults calculated form Equation (7)-(9), campared with the measurements of a prism coupler and SEM.

We cannot evaluate the results of Δd calculated from Equation (8) because it is not possible to measure the remaining Ag film after it is heated and oxidized in the oven. However, from Table 2, the waveguide depths calculated from Equation (9) show very good agreements with the results measured by the prism coupler and the SEM results. In future work, we can use Equation (9) to predict the waveguide depth of planar waveguides so that the time and cost spent on measurements can be avoided.

For channel waveguides, Equation (4) and (5) have to be solved numerically. We can refer to Ref. [19] for an evaluation of the waveguide profile $d(y)$ and the source film thickness $s(y)$ during ion exchange, starting with a 30-μm-wide Ag stripe in Figure 3-9.

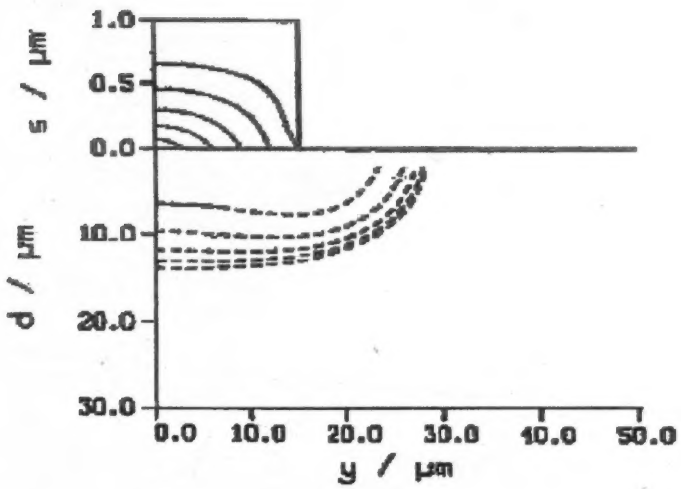

Figure 3-9 Evaluation of waveguide profile *d(y)* and source film thickness *s(y)* during ion-exchange in Ref. [19]. Each *d(y)* curve corresponds to one *s(y)* curve.

3.5 Characterizations of ion-exchange waveguides

3.5.1 Waveguide side diffusions and surface swells

Figure 3-10(a) shows a SEM image of a waveguide fabricated with a 21 um mask opening. The substrate is tilted so that both the top and the side images can be shown. The stripe on the center top of the waveguide indicates where the ion-exchange mask opening was. This area is visible because the glass surface was damaged when Ag^+ ions were driven through the mask opening. A magnified image in Figure 3-10(b) shows the rugged surface at the mask opening after the ion exchange. The side diffusion is a result of the bent electric field line (Figure 3-2(b)) due to the existence of an ion-exchange mask. The side diffusion size is approximately the depth of the waveguide. But it is apparently varies with substrates because the electric field is solved from the parameters of the glass structure.

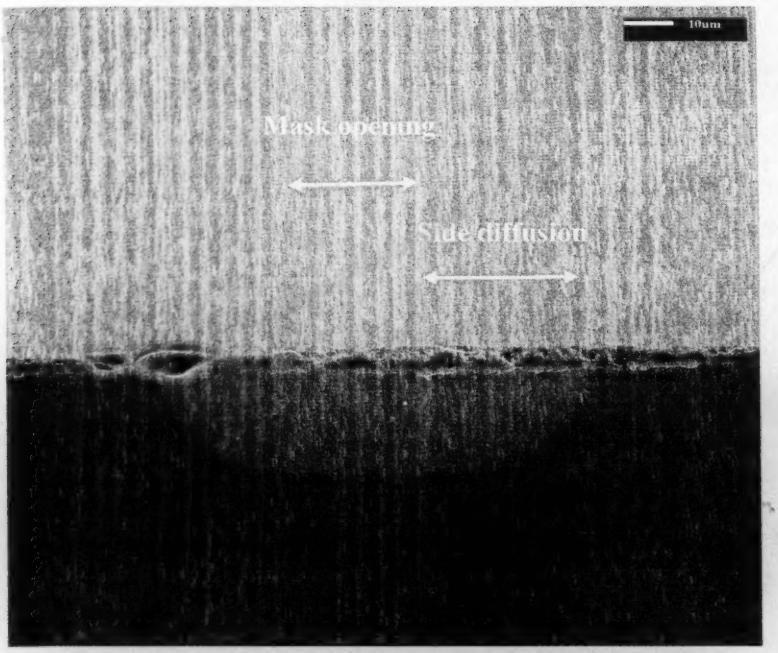

(a)

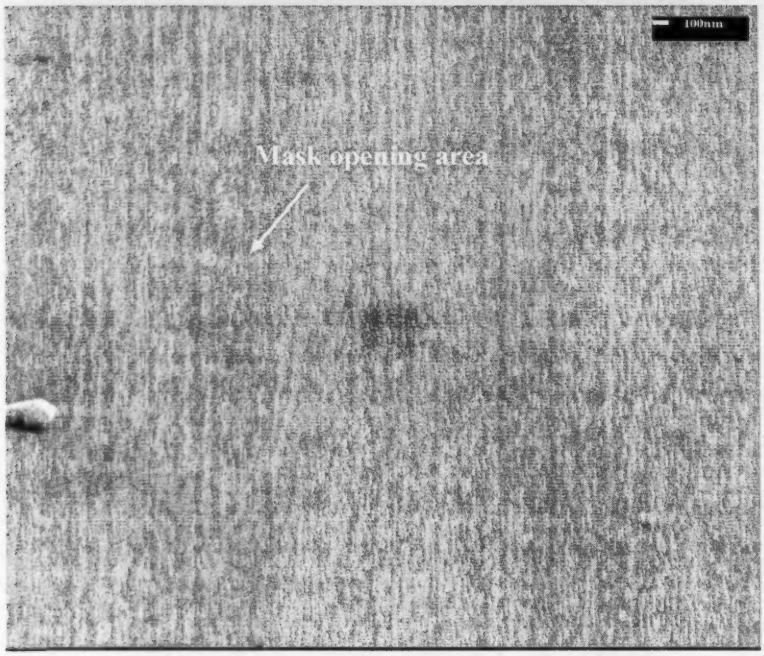

(b)

Figure 3-10 (a) SEM image of a channel waveguide. The stripe on the center top of the waveguide is where the mask opening was. The size of side diffusion is approximately the depth of the waveguide. (b) Substrate surface changed by the ion exchange in the mask opening area

Similar ion-exchange parameters were used on one Corning 0211 substrate (380-385°C, 35 V/mm, 40 min) and one Schott borofloat substrate (380-395°C, 35 V/mm, 40 min). The waveguide profile on Schott substrate (Figure 3-11(a)) is more like a semi-circle, which is close to the results of Ref. [22] on BF450 glass substrates. The ion exchange on the Corning substrate generates shallower waveguides than that on Schott substrate, and more side diffusion, as seen in Figure 3-11(b). The waveguide profiles achieved on the Corning substrate agree with most literature and the earlier research in our group [25]. A small mask opening (11 μm) results in a well-like waveguide side profile, while a bigger opening (21 μm) results in a saddle-like profile.

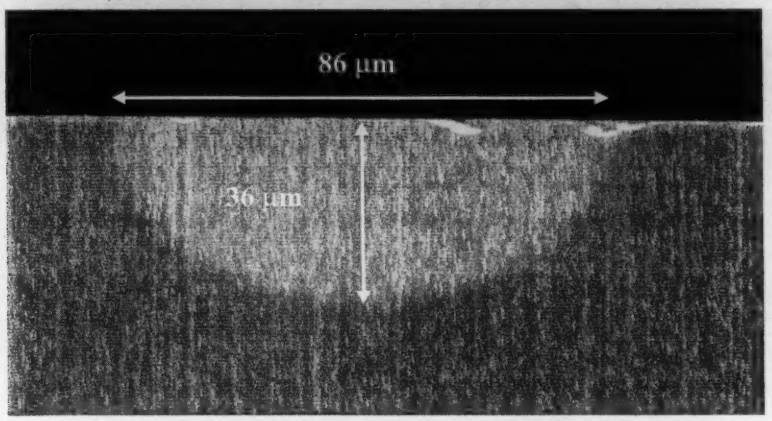

(a)

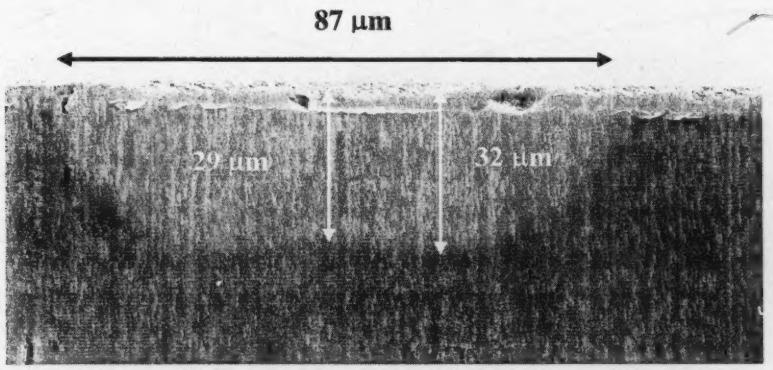

(b)

Figure 3-11 (a) SEM Image of a waveguide made on Schott borofloat glass with a 21 μm opening. (b) SEM image of a waveguide made on Corning 0211 glass with a 21 μm opening.

Ag atoms are larger than Na atoms. When Ag^+ ions substitute Na^+ ions in the glass network, the glass expands and swells the surface. The size of the swell depends on the waveguide depth and the type of glass. As shown in Figure 3-12(a), there is a 130 nm swell when a 32 um deep waveguide is formed on a 0211 substrate. But there is a 60 nm swell (Figure 3-12(b)) on a 36 um deep waveguide on a Borofloat substrate. The bigger the swells, the more they affect the bonding process.

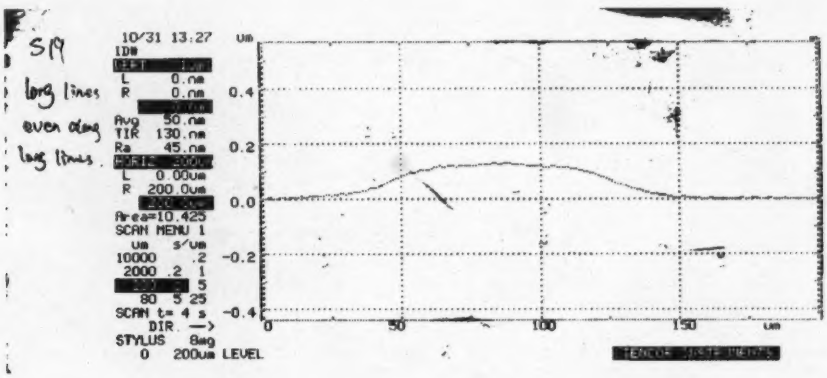

(a)

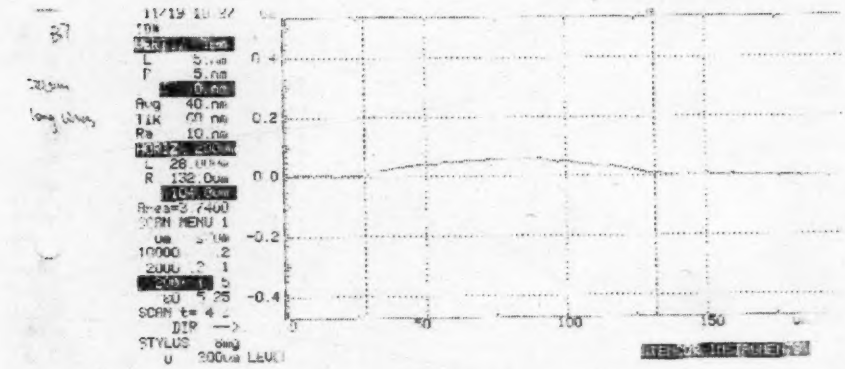

(b)

Figure 3-12 (a) Profilometer plot of a 130 nm swell of a 32 μm deep waveguide on a Corning 0211 substrate. (b) Profilometer plot of a 60 nm swell of a 36 um deep waveguide on a Schott borofloat substrate.

From the results above, Schott borofloat is seen a better substrate to fabricate ion-exchange waveguides. Using same ion-exchange parameter, waveguides fabricated on Schott borofloat substrate have deeper depth and smaller surface swell, which has less effect to the bonding process. Also, there is

no observable yellow color on the waveguides fabricated on the Schott Borofloat substrate, indicating possibly low waveguide losses. In addition, compared with the 0.53-mm-thick Corning 0211 substrates, the 1.1-mm-thick Schott borofloat substrates can stand rougher handling in the process and in the applications.

3.5.2 Waveguide losses

Waveguide losses can be broken down into coupling loss, propagation loss, and scattering loss. Coupling loss may be the largest part because of the mismatch between the circular input fiber and the semicircular shaped waveguide, the distance between them and reflections from the fiber and waveguide ends. The scattered light is emitted from the top of waveguides, which is exposed to the air. The scattered light is influenced by glass cracks from ion exchange, the surface roughness and cleanliness, and also by the amount of Ag atoms in the waveguides. Assume that the scattering is proportional to the local intensity of the propagating light, the following method to measure the waveguide propagation loss can be used.

The pictures of light propagation in a 4-cm-long waveguide and the output light taken by a CCD camera with a focus range and a shutter to control the amount of input light are shown in Figure 3-13(a) and (b) respectively. In Figure 3-13(a), the laser light is confined very well in the waveguide. The bright glow at the coupling point at the left side of the picture is due to the reflection of light at the waveguide end. An index matching material should be able to reduce the reflection and the coupling loss. Also the output point at another end of the waveguide has a strong glow because of the emitted light from the waveguide and possibly an improper polished end. Therefore, to calculate the propagation loss, these two sections close to both ends should not be taken into account. From the top of the waveguide, the scattered light is attenuated gradually as the light propagates. However, cracks, dirt and rough surface affect local values of the scattering light. Sometimes these effects are very phenomenal so that the loss measurement is influenced dramatically.

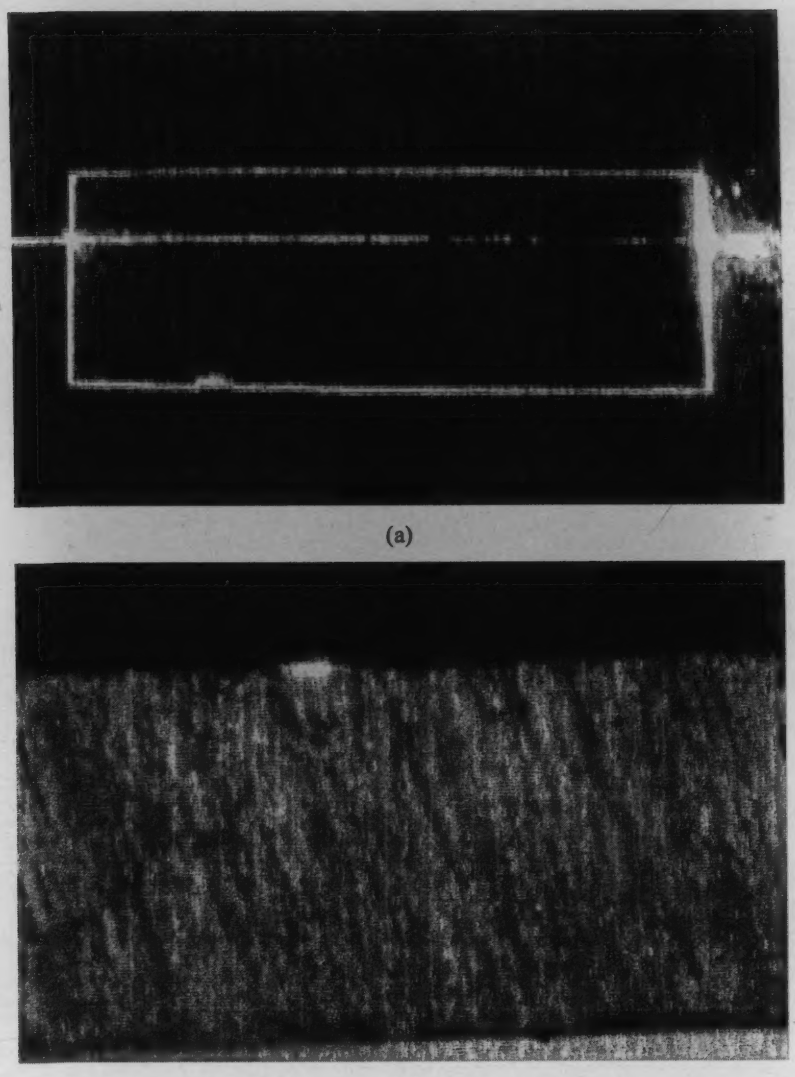

Figure 3-13 (a) Top view of laser light propagating in a 4-cm-long waveguide. An optical fiber is coupled to the waveguide from the left. (b) Side view of laser light at a waveguide end.

A scheme of the setup used to measure the scattered light is shown in Figure 3-14. He-Ne Laser light at 633 nm is focused on one end of a piece of glass optical fiber with a 50-μm-diameter core. The other end of the optical fiber is butt-coupled to an end-polished waveguide. (We have also used other input methods including using a laser diode at 633nm instead of the He-Ne laser, focusing the He-Ne laser light directly onto the waveguide end, and using a single mode laser at 673nm with an optical fiber connected directly to it.) The PMT pick-up fiber is

mounted above the waveguide but not touching it. The scattered light is measured point by point by moving the PMT pick-up fiber along the waveguide. Propagation loss is calculated from the attenuation of the scattered light. The input fiber, the substrate with waveguides, and the PMT pick-up fiber are mounted on 3-dimentional micropositioners to achieve accurate adjustments.

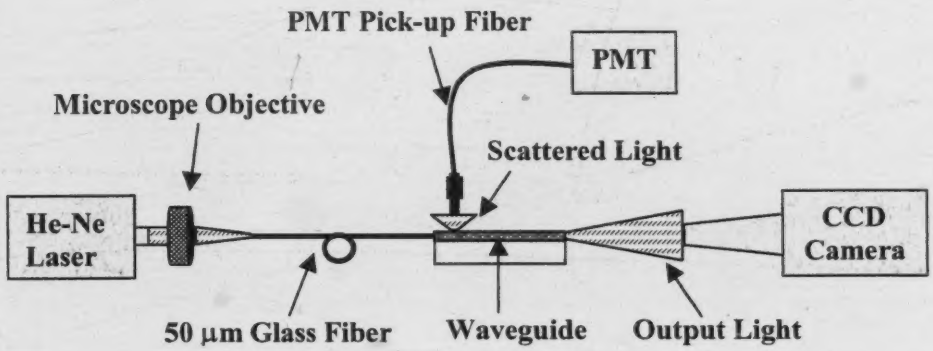

Figure 3-14 Schematic setup of waveguide propagation loss measurement.

We measured the scattered light from the waveguides with the yellow color. Figure 3-15 shows the measurement of an approximately 4-cm-long waveguide at 1 mm intervals. Picking out the measurements from the first and last 5 mm, fitting the decibel data into a straight line, the propagation loss is found to be 3.4 dB/cm at 633 nm. The measurement results from other waveguides on the same or a different substrate using this method show the propagation loss at a range of 3-8 dB/cm at 633 nm. However, the fitting in Figure 3-15 is still not realistic even though more points are discarded at two ends. The PMT tends to pick up some light emitted from the optical fiber directly at the front part of the waveguide because of the mismatch of optical fiber and the waveguide.

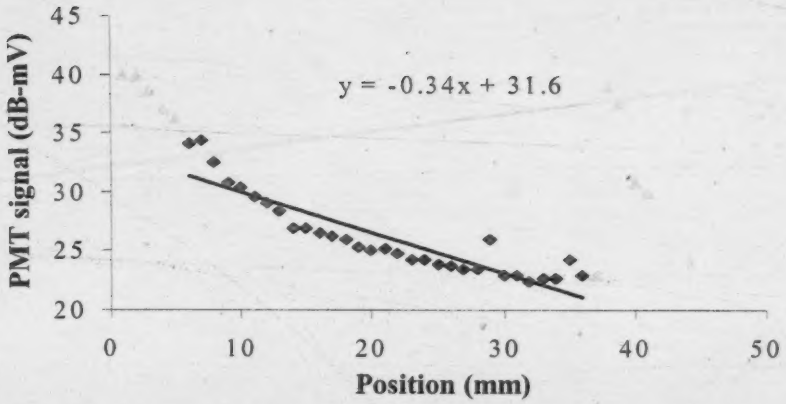

Figure 3-15 Measurement of scattered light at 1 mm intervals with waveguide facing up. Vertical units are 10log(PMT signal in mV). The data except the first and last 5 mm are fitted into a line. Attenuation is 3.4 dB/cm.

To block the excess light from the optical fiber, the substrate was turned so that the waveguides were faced down. The light incident outside of the waveguide shone on the substrate holder and was reflected out of the PMT capture range. The same measurements were conducted, and the attenuation of two straight waveguides is 2.4 dB/cm and 3 dB/cm respectively at 633 nm, as one shown in Figure 3-16. The bigger variation and lower power measured, compared with those in Figure 3-16, can be understood from noting that light has to go through the glass substrate to enter the PMT pick-up fiber, and the backside of the substrate is rougher than the front side as a result of Na driven out of glass during ion exchange.

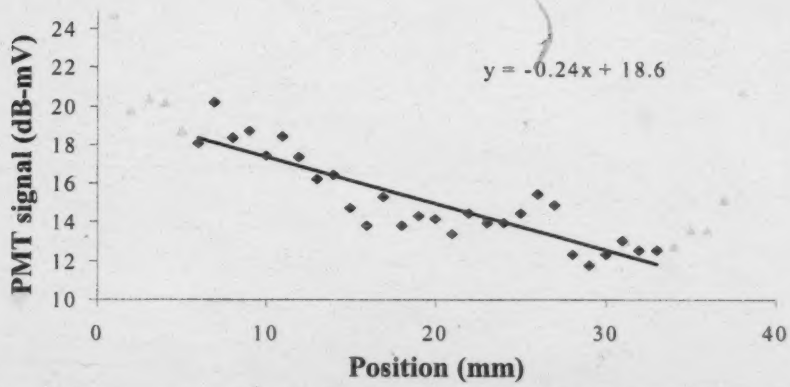

Figure 3-16 Measurement of scattered light at 1 mm intervals with waveguide facing down. Vertical units are 10log(PMT signal in mV). The data except the first and last 5 mm are fitted into a line. Attenuation is 2.4 dB/cm.

We also measured the scattered light across a waveguide, as shown in Figure 3-17. The resolution of the measurement is 1mm, the same as the diameter of the PMT pickup fiber. This figure shows that there is essentially no light outside the waveguide region.

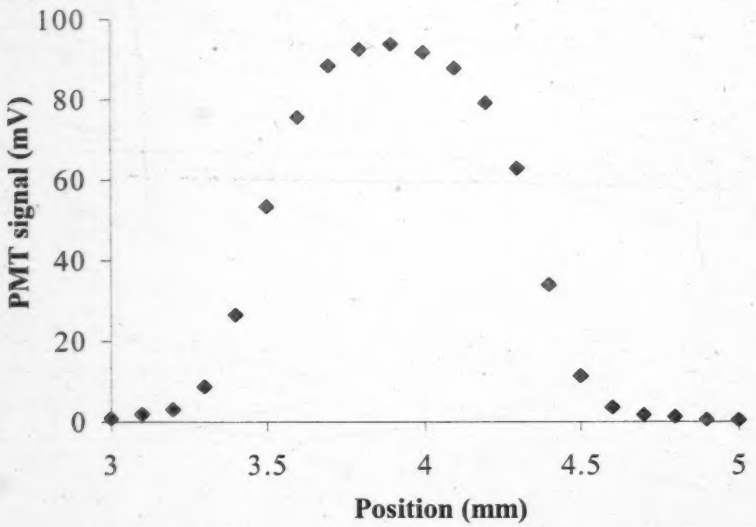

Figure 3-17 Measurement of scattered light across a waveguide.

Compared with the propagation losses in literature, such as 0.2 dB/cm in Ref. [27] and less than 0.1 dB/cm in Ref. [22], the propagation losses of these waveguides are large. The reason may be that the waveguides measured all have yellow color on them, which is considered to be the main source of the scattering loss in ion-exchange waveguides. However, this is not a serious problem because the lengths of waveguides on centimeter-scale biochips are short. The other losses such as the coupling loss may be larger factors instead.

The other waveguides fabricated on one borofloat substrate don't show visibly yellow color. However, this substrate was broken accidentally in the NanoFab. The longest waveguide on the broken pieces was only 1 cm long, which was not suitable for a loss measurement.

4 BIOCHIPS WITH INTEGRATED MICROCHANNELS AND WAVEGUIDES

4.1 Integration of microchannels and waveguides on a single substrate: two approaches

The goal of this research is to integrate ion-exchange waveguides and glass-etched microchannels on a single substrate. There are two possible ways to integrate waveguides and microchannels: fabricating waveguides on a substrate with microchannels, or vice versa. We conducted experiments on both possibilities and evaluated the feasibility of each method.

A dual-function quartz mask was designed for both the waveguide and microchannel fabrication. Refer to Appendix 3 for the detailed layout of the mask. By using this mask, four types of intersections, as well as their mirror images, were fabricated: (1) straight waveguide intersecting a straight microchannel, (2) Y-shape waveguides intersecting a straight microchannel, (3) curved waveguides intersecting U-shape microchannels, and (4) eight waveguides distributed 20^{o} apart around a circular chamber in the center of a straight microchannel.

4.1.1 Fabrication of waveguides on a substrate with microchannels

One Corning 0211 substrate with 25-μm-deep microchannels fabricated in the NonaFab, and 5 Schott borofloat substrates with 20-μm-deep microchannels from Micralyne Inc. were used in this experiment. After Cr was sputtered as the ion-exchange mask, and HPR 504 photoresist was spun on, exposed and developed for lithography, we noticed some unusual patterns generated around the microchannels.

First, the photoresist tended not to cover the channel walls and the surface close to the channels. The blank areas on the two sides of the microchannel, vertical dark strips in Figure 4-1(a), had no photoresist; neither did the horizontal waveguide stripe. Secondly, the photoresist on the side towards the spinning center, the left side of the channel in Figure 4-1(a), was twice as thick as that on

the side far from the spinning center, the right side of the channel. The layered fringes indicate the variation of the photoresist thickness. Consequently, while the photoresist on the right side was developed properly, the thicker photoresist on the left side was under developed. Thirdly, thicker photoresist filled in the channel than that spreads on the surface. As a result, the photoresist at the intersection of the waveguide and the microchannel was too thick to develop by the standard process. In the next process step, Cr was etched away where there was no photoresist protection. Therefore, the substrate surface in the dark area in Figure 4-1(b) was exposed to ion exchange. Chromium at the intersection was not etched completely due to the protection of the under-developed photoresist.

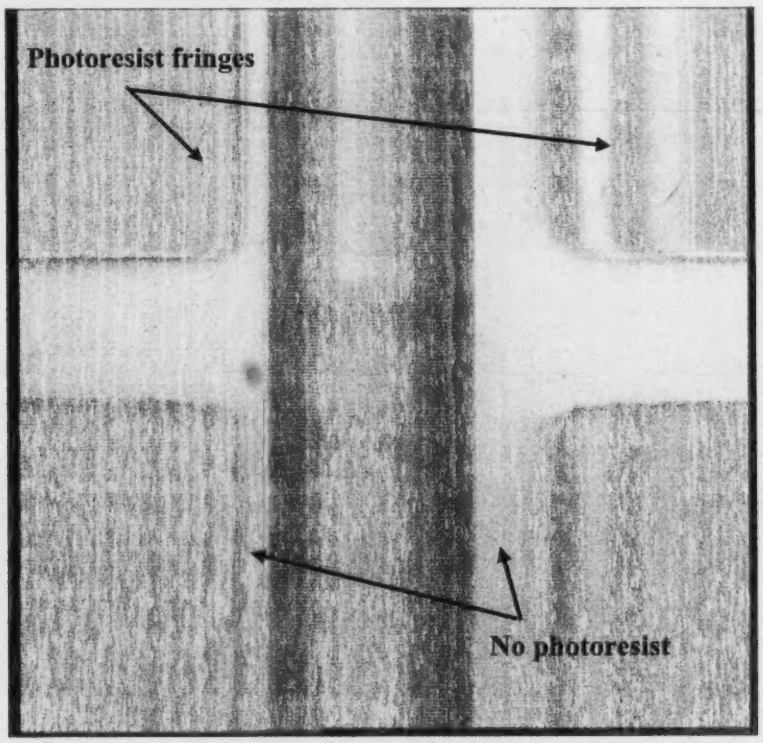

(a)

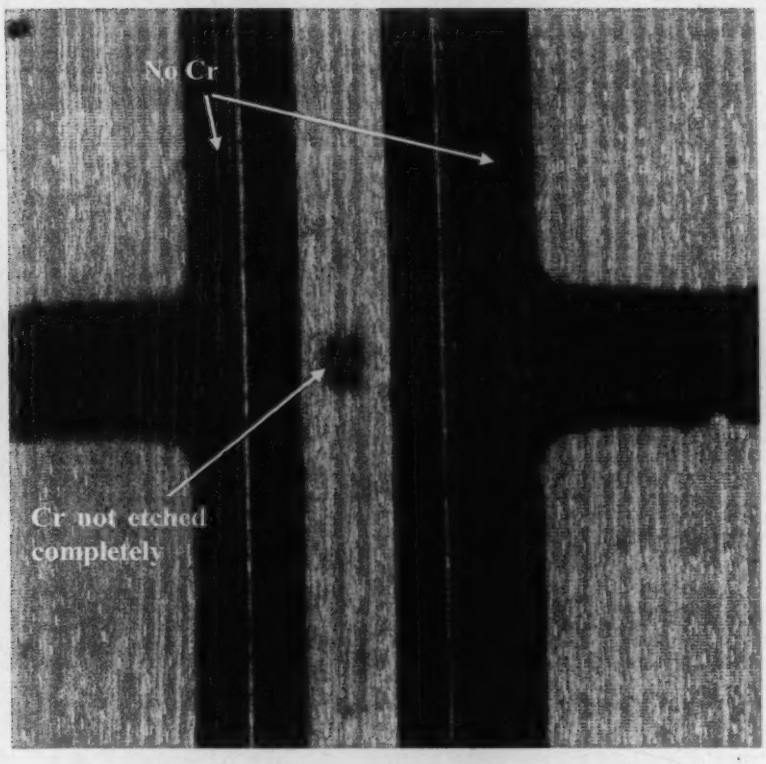

(b)

Figure 4-1 Intersection pictures of microchannel walls (vertical dark strips) and waveguide patterns (horizontal strips). (a) No photoresist on the surface close to the microchannel. Photoresis on the left side of the channel is thicker than that on the right side. (b) Cr (white) on the surface close to the microchannel is etched. Cr at the intersection is not etched completely.

The ion-exchange process was carried out on four of these substrates. However, these experiments were conducted before the Cr mask problem was solved. So Ag^+ ions migrated into the whole substrates including the channel bottoms. Figure 4-2 shows a SEM image of 50-μm-deep ion-exchange at a 20-μm-deep channel bottom. If the Cr mask had worked for these substrates, ion-exchange would not have occurred on the channel bottoms.

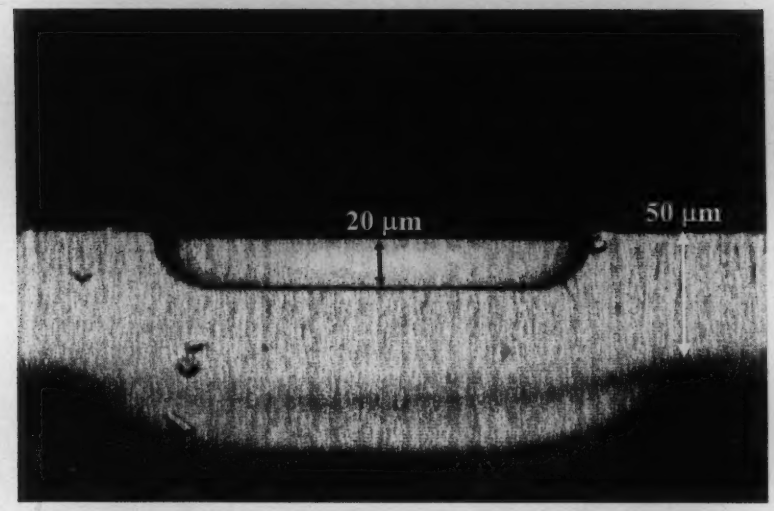

Figure 4-2 SEM image of 50-μm-deep ion-exchange at a 20-μm-deep channel bottom.

It may be possible that, by slowing down the spread and spin speeds of the photoresist for lithography the surface without photoresist covered in Figure 4-1(a) would become smaller. When the spread and spin speeds are slow enough, eventually, the whole channel including the surface close to it would be covered by the photoresist. Of course, the thickness of the photoresist spread on the surface would be increased with slowing the spread and spin speeds. Correspondingly, all the other related lithography parameters, including the time for hard bake, exposure, and developing, would have to be adjusted. From this point of view, the other method of etching microchannels into substrates with waveguides was seen as a better alternative.

4.1.2 Fabrication of microchannels on a substrate with waveguides

This method was tried on two Corning 0211 substrates and one Schott borofloat substrate, all with pre-fabricated ion-exchanges waveguides. A few phenomena were observed while microchannels were fabricated on these substrates.

I. The change of glass composition affects the glass etching speed

The ion exchange process, in which Na^+ ions in the glass are replaced with Ag^+ ions, changes the glass composition, and so changes the glass

etching speed where microchannels cross waveguides. If Ag^+-ions-rich glass has a higher etching speed than Na^+-ions-rich glass, dents will form at the intersections. Otherwise, bulges will form. By carefully checking the intersections with a Tencer Alpha Step profilometer, a ZYGO optical profilometer and a SEM, we have found that Ag^+ ions slow down glass etching, and the size of the bulges formed at the intersection is 3-4% of the channel depth on both Corning 0211 and Schott borofloat substrates.

Figure 4-3 shows the scanning result of an optical profilometer along a 28-μm-deep microchannel (Figure 2-3) at its intersection with a 36-μm-deep 86-μm-wide waveguide (Figure 3-11(a)). The height of bulge is about 1 μm, and the width of the bulge is about 90 μm, which agrees with the waveguide width.

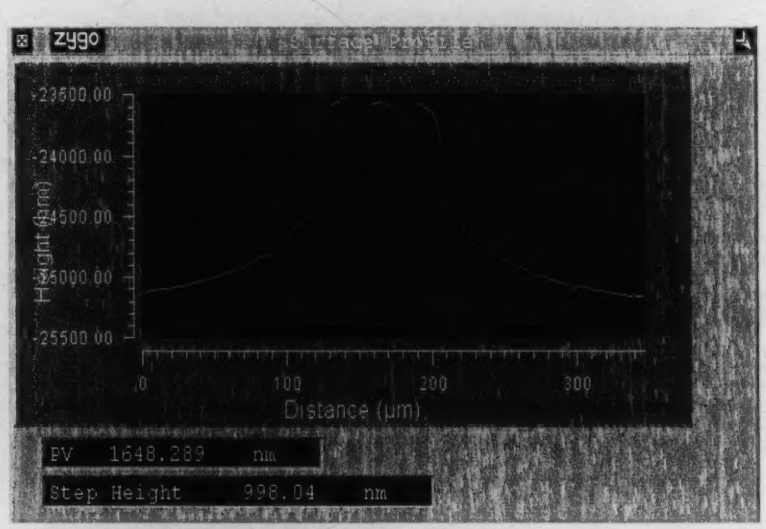

Figure 4-3 Optical profilometer scanning of a bulge at the intersection of a 28-μm-deep microchannel and an 86-μm-wide 36-μm-deep waveguide.

We have also noticed another interesting phenomenon associated with glass composition change. In Figure 4-3, there are two trenches about 30 μm apart in the middle of the bulge, which scale is close to the size of the 21-μm mask opening that is used for making this waveguide. Figure 4-4(a) and (b) show SEM images of the same intersection scanned in Figure 4-3.

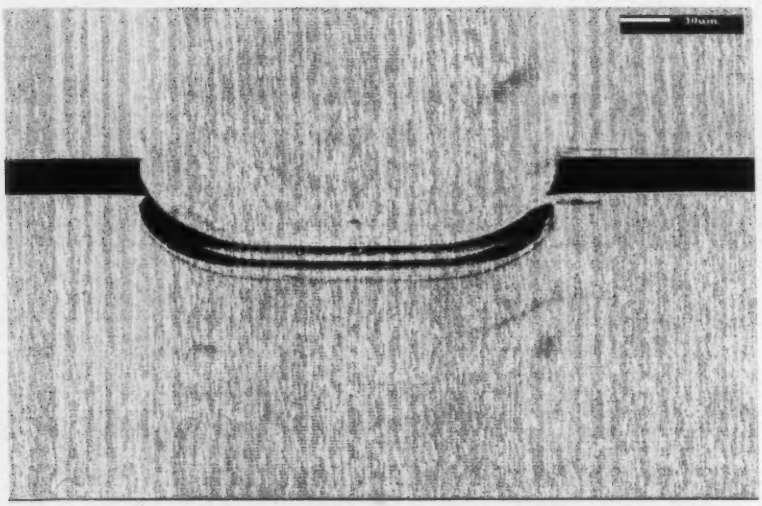

(a)

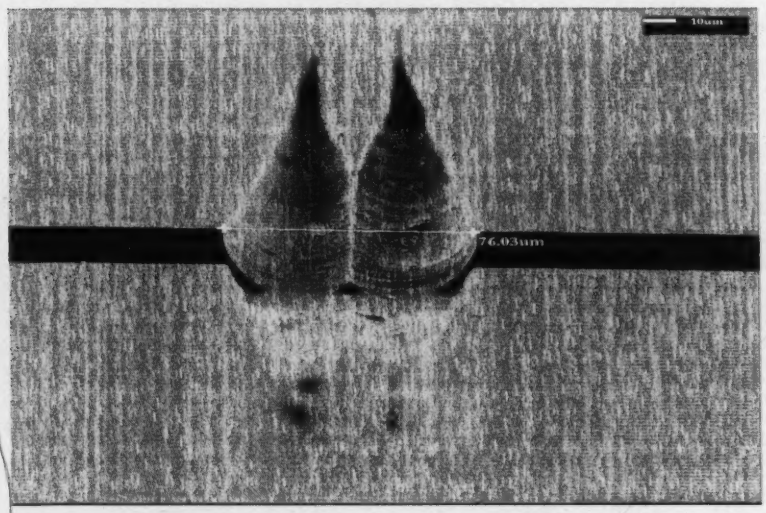

(b)

Figure 4-4 SEM images of trenches formed at an intersection. (a) microchannel (vertical) and waveguide (horizontal). (b) microchannel (horizontal) and waveguide (vertical).

We explain this phenomenon as follows. As discussed in Chapter 3, some ion-exchange waveguides exhibit a yellow color because Ag^+ ions are changed back to Ag atoms at the edges of the ion-exchange mask openings. During etching of the microchannels, Ag atoms at the waveguide surface are etched first where they contact the glass etchant directly because the glass etchant contains nitrate acid, which attacks Ag atoms aggressively. Shallow trenches are then formed in the waveguides at the intersections, and following

these paths, the glass etchant continues to attack other Ag atoms close to the intersections.

Another two intersections on a different substrate confirmed our analysis. Two curved microchannels were patterned at both sides of a U-shape waveguide. Because of misalignment in the process, the end of one microchannel pattern intruded into the waveguide, while the end of the other microchannel pattern was separated from the waveguide. After the microchannels were etched, trenches were found at the intersection where the microchannel was etched into the ion-exchange mask opening area, as shown in Figure 4-5(a). On the other side, the microchannel extended into the waveguide due to the undercutting of glass etching, but did not contact the ion-exchange mask opening area. As shown in Figure 4-5(b), no trench occurred to this intersection.

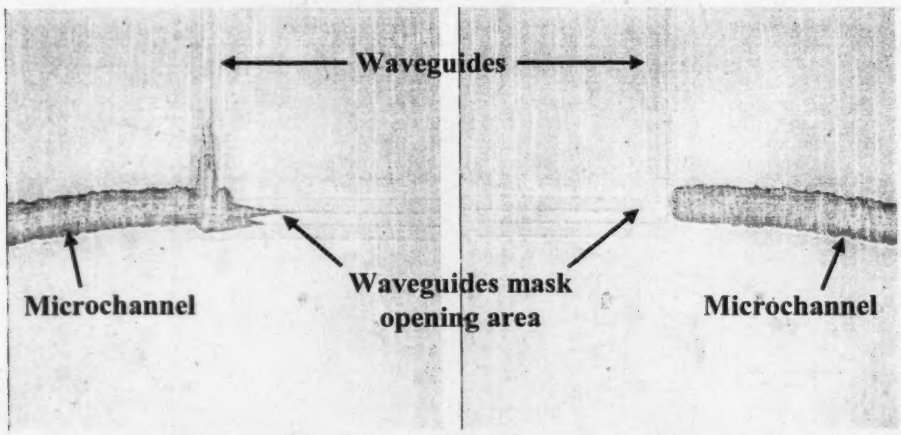

Figure 4-5 (a) Trenches occur when the curved channel is etched into the ion-exchange mask opening area.(b) No trench occurs when the curved channel is not etched into the ion-exchange mask opening area.

Reducing the change of Ag^+ ions to Ag atoms in waveguides is one solution to resolve the trench problem. Alternatively, we propose an intersection design by leaving enough space between input and output waveguides for the side diffusion of waveguides and the side etch of the microchannel, which is etched between two waveguides. As an example, in Figure 4-6 we assume 30-μm-deep waveguides and microchannels are

fabricated with 10-μm-wide openings for both the waveguide and channel masks. At each end of the waveguides, there will be approximately 30 μm side diffusion when a 30 μm depth is generated. According to the etching result in Figure 2-3, the microchannel width is estimated to be approximately 90 μm. In total, a 150-μm-wide space is left between the two waveguides openings on the waveguide mask. One limitation of this design is that great effort needs to be paid to the alignment of the microchannels and waveguides.

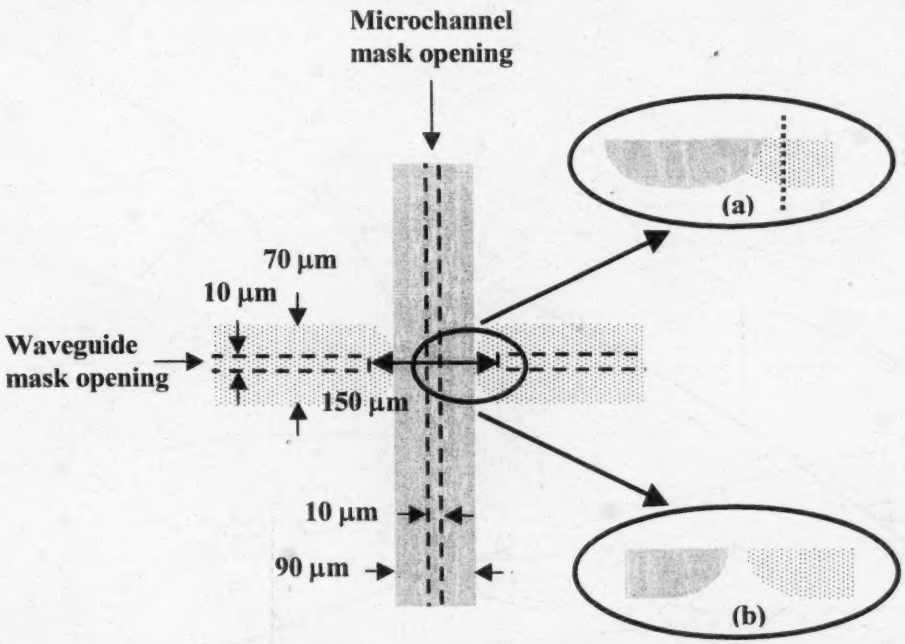

Figure 4-6 Proposed intersection scheme to avoid trenches etched in the waveguides.

Considering the other offsets from lithography and subsequent etchings, the microchannel can overlap some of the waveguide region without generating trenches as long as the microchannel is not etched into the ion-exchange mask opening area, (magnified area (a) in Figure 4-6). However, we may expect that the light is emitted into and detected from the microchannel at different angels as the end shapes of the input and output waveguides are changed.

On the other hand, if the microchannel is not etched into contact with the waveguides (magnified area (b) in Figure 4-6), the intersection generated will be similar to the structure studied in Ref. [9], where a dike is formed between the waveguide and the channel to prevent leakage. Figure 4-7 shows a top view of a beam-propagation method (BPM) simulation of light from a 24-μm-wide waveguide (4-μm-high) coupled into a 500-μm-wide channel through a 10-μm-wide dike. The light starts to diverge while it goes through the dike. The numerical aperture is increased by approximately 5%, which is believed a negligible change.

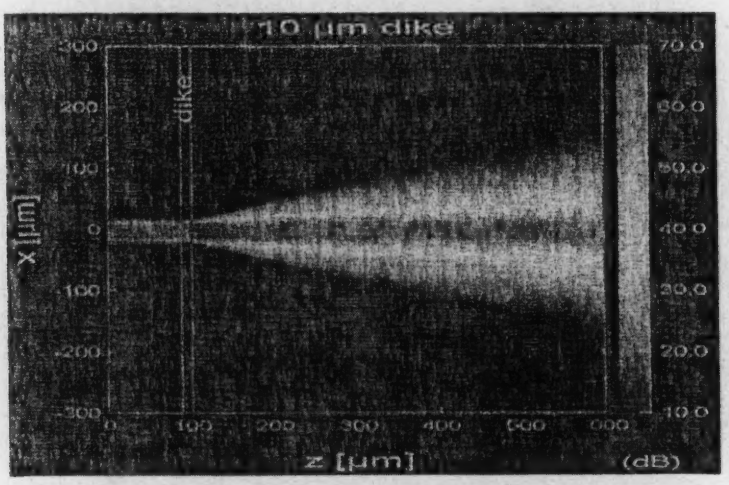

Figure 4-7 BPM simulations in Ref. [9] of light from a 24-μm-wide waveguide (4 μm high) coupled into a 500-μm-wide channel through a 10-μm-wide dike.

II. The surface condition affects lithography

During lithography, the microchannel mask cannot have intimate contact with the substrate because of the waveguide swells. Divergence and diffraction of UV light may occur at the edges of the mask and undercut the photoresist, contributing to a lateral expanding of the microchannel width. Another factor affecting lithography is that the gap between the microchannel mask and the substrate is not even over the whole surface, because the substrate is bent by a few heating processes while making waveguides. Consequently, the photoresist is unevenly exposed and developed over the

whole substrate, and glass islands may form in the microchannels under the protection of some under-developed photoresist.

III. Phase separation

Elevated temperatures in the waveguide process separates borosilicate glass into different phases, a silica rich phase and an alkali borate rich phase [29]. Since the alkali borate phase has a faster dissolving speed in the glass etchant than the silica rich phase, glass can be leached to remove the alkali borate rich phase and leave a silica skeleton. We observed porous and smooth microchannel bottoms etched on substrates with and without the waveguide process respectively. However, there is no further evidence to prove the effects of the phase-separated glass on the microchannel performance.

4.1.3 Alignment of waveguides and microchannels

In both methods discussed in the first two sections, the alignment of waveguides and microchannels is the key to achieve proper intersections. We adopted the three-group alignment marks designed in earlier research of our lab and applied them to each corner of the waveguide and microchannel masks. To achieve tolerant intersections, at least two groups of the alignment marks need to be aligned with an assistance of the microscope on the AB-M mask aligner.

If we fabricate microchannels on the substrate first, the alignment marks are etched into the substrates like the other microchannels. The alignment marks are easy to recognize because they are etched very deep. If we fabricate waveguides on the substrate first, the alignment marks are diffused into the substrate like the other waveguides, as sown in Figure 4-8. As discussed in Chapter 3, they have different refractive indices and swells on the surface, and can be observed under a microscope. However, the contrast of swelling to the background is reduced after metal films are sputtered and photoresist is coated on the substrate to fabricated microchannels. From our experience, the alignment marks were recognizable with 220 nm metals and 1 μm photoresist on 130 nm swells. But with similar coatings on 60 nm swells, the alignment marks were barely seen. In this case, extra steps

were introduced to remove photoresist and metals at each corner of the substrate using a cleanroom swab, dipped into the appropriate etchants.

Figure 4-8 Picture of three-group alignment marks diffused into one corner of the substrate.

4.2 Completion of integrated biochips

As discussed in Chapter 2, to complete a biochip, cover plates with via holes were bonded on the substrate with integrated waveguides and microchannels, and the edges of the biochip were cut and polished. In this research, we completed five biochips with integrated waveguides and microchannels, and studied how the existence of waveguides affected the bonding process and how waveguides were changed after bonding.

4.2.1 Interaction of the bonding process and waveguides

Similar to but smaller than regular contamination, waveguide swells act like also defects between the bonded glass parts. There were no actual Newton rings, which usually indicate the existence of particles between the bonded glass, observed around the waveguide swells. The light color reflected from the region

around the waveguide swells was slightly different to that from the flat surface. The region of different reflected light on 60 nm swells was barely visible. On 130 nm swells, it was about five times of the waveguide width. It became larger where the waveguides had a higher density, for example, in the Y-shape waveguide area. However, the light propagation result of a Y-shape waveguide shows that there was no light leakage caused by the above effect.

On the other hand, the bonding process affected the waveguides by diffusing the waveguides deeper into the substrate and the cover plate. Comparing the waveguide after a 3-hour bonding at 300°C (Figure 4-9) with the waveguide made with the same mask opening on the same substrate before bonding (Figure 3-11(a)), the former was diffused approximately 2 μm more, which was about 5% of the original waveguide depth.

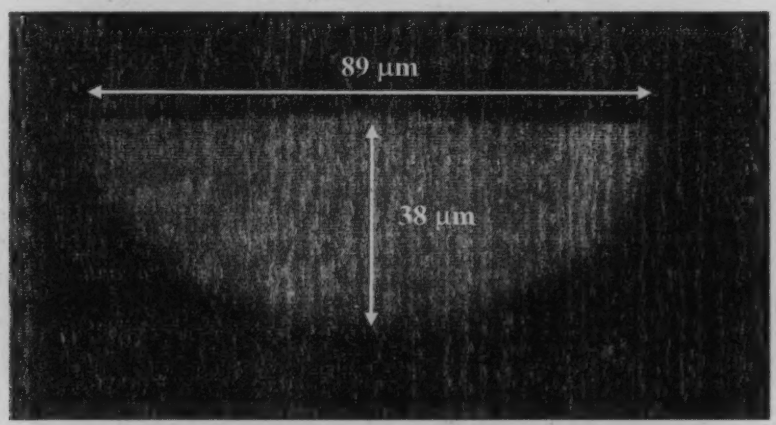

Figure 4-9 SEM image of a waveguide after bonding.

A 1-2 μm diffusion into the cover plate has been found only at the ion-exchange mask opening area, as shown in Figure 4-10. This may be explained from the view of the glass boundary energy. Normally, when two pieces of glass contact each other, two boundary energies need to be overcome to move ions from one to the other. However, when Ag^+ ions are driven into the substrate through the ion-exchange mask opening, the glass network is broken through and the boundary energy is changed in this area. As a result, it is easy for Ag^+ ions at the ion-exchange mask opening area to move out of the glass at an elevated

temperature, and overcome the other boundary energy to diffuse into the cove plate by a thermal diffusion. The Ag film on this substrate was not used up during the ion exchange, so the damage was not caused by the ion-source depletion, which was usually responsible for the surface damage as discussed in literature.

Figure 4-10 Diffusion into the cover plate in the mask opening area during bonding.

4.3 Detection of fluorescence in integrated optical biochips

The integrated biochips fabricated using the method in Section 4.1.2 were tested optically. Laser light was focused directly onto one end of a Y-shape waveguide, which was split to two waveguides and intersected with a straight microchannels at the two branches. The laser light was confined very well in the two branches of the Y-shape waveguide until it struck on the microchannel walls, resulting in two bright spots, as shown in Figure 4-11(a). The output waveguides on the other side of the microchannel picked up some light (two faint light trails in Figure 4-11(a)) and directed it out of the biochip, appearing as another two spots

at the ends of the output waveguides. Similarly in Figure 4-11(b), a curved waveguide directed the laser light into a U-shape microchannel. After travelling along the 1 mm microchannel, little light was picked up by the output waveguide at the down side of the U-shape microchannel. These qualitative results above demonstrate the potential of integrating waveguides and microchannels.

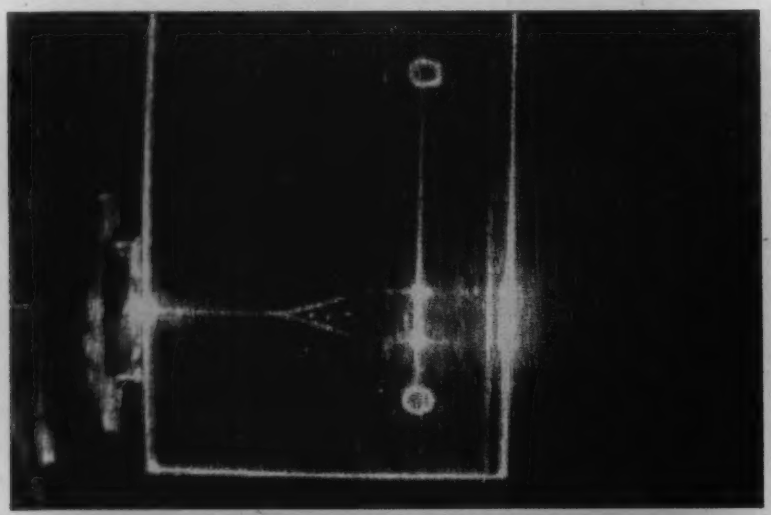

(a)

(b)

Figure 4-11 Optical tests on integrated biochips. (a) Laser light travels in a Y-shape waveguide and shines into a straight microchannel. (b) Laser light travels in a curved waveguide and shines into a U-shape microchannel.

Fluorescence signals were measured on the integrated biochip with the Y-shape waveguide in Figure 4-11(a) by another researcher in our lab. A dye solution, Nile Blue 690 from Exciton Inc., with an absorption peak at 628nm and an emission peak at 660nm was injected into the straight microchannel through one via hole. The PMT pick-up fiber was mounted above the microchannel and moved along the microchannel across the two intersections. When the microchannel was empty, only the scattered laser light was picked up by the PMT, the maximum signal was approximately 50 mV, as shown in Figure 4-12. After the dye solution was injected, the PMT signals were increased approximately 5-10 times. Also note that the signals at two intersections are not equal. This may be a result of a faster evaporation of the dye solution at the bottom intersection as it is closer to the opened reservoir.

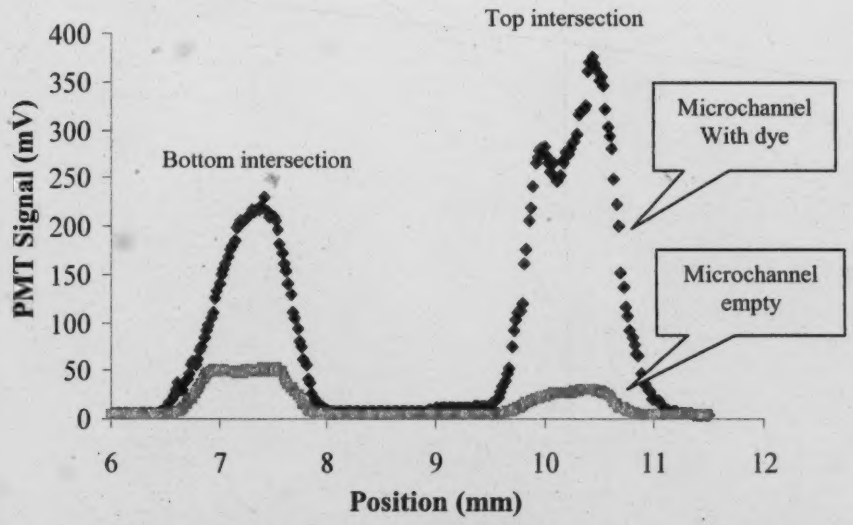

Figure 4-12 PMT measurements at intersections of waveguides and microchannels when the microchannel was empty and injected with a dye solution.

Measurements from the side of the output waveguides were also attempted, however, resulting in no distinguishable signal from the background noise so far. The reason may be that the coupling of the fluorescence to the output waveguides is affected by the trenches formed at the intersections. However, this fluorescence detection experiment proves that laser light can be delivered to specific points in a microchannel through optical waveguides fabricated on the biochip.

5 CONCLUSIONS

The goal of this thesis was develop a method of fabricating optical waveguides and microchannels in the same glass biochip, and detect fluorescence signals from fluids in the microchannels using a computer-controlled optical measuring system. Through the research in this thesis, we conclude our achievements as follows.

- The glass-etched microchannel process was improved and the fabrication of glass biochips with enclosed 20-30 μm deep glass-etched microchannels was implemented in the NanoFab in the University of Alberta. The fabricated biochips were tested by driving fluid in the microchannels using a syringe, and no leakage was observed.
- The main challenge of the ion-exchange mask problem was conquered, and 30-40 μm deep channel waveguides were fabricated. The relations of the ion-exchange parameters, the resulting currents, and waveguide depth were studied. The issues related to surface swells, side diffusions and waveguide coloration were discussed. The waveguide propagation loss was measured on the waveguides with a yellow color, resulting in approximately 0.3 dB/mm.
- Two methods were demonstrated to integrate ion-exchange waveguides and etched microchannels on glass substrates. In each method, the problems at the intersections of waveguides and microchannels were addressed and the solutions were proposed correspondingly. The preferred procedure at this stage is to fabricate waveguides in the glass substrates first and then etch microchannels. Five 2x3.5 cm^2 integrated optical biochips were fabricated using this method. The delivery of light to the microchannels was demonstrated and the fluorescence signals from dyed fluid in the microchannels were detected from the top of the microchannels.

For future research in this area, the problems and suggestions to be addressed are:

- The waveguide losses are still of concern. Ag^+ ions changing back to Ag atoms are responsible for the yellow color in the waveguides and the scattering loss. To reduce the ion-exchange waveguide losses, it may be required to use lower temperatures to fabricate waveguides, according to Ref. [20], to use Ag strips instead of using a patterned ion-exchange mask, as suggested in Ref. [27], and to use Schott borofloat substrates or choose other substrates with lower reported losses, such as BF450 in Ref. [22]. We should also consider buried waveguides because of their low scattering losses and symmetric refractive index profiles that can match well to optical fibers. Ref. [30] and [31] both proposed a single-step field-assisted ion-exchange method to fabricate such buried waveguides.
- Photoresist does not stay on the substrate surface close to the microchannels when we fabricate waveguides on the substrates with microchannels. Experiments need to be conducted on the photoresist coating techniques and adjusting the lithography parameters.
- The trenches formed at the intersections of waveguides and microchannels affects the light propagation and coupling. To prevent the waveguides from being attacked when microchannels are etched on the substrates with waveguides, we suggest using the proposed mask layout.

REFERENCES

[1] D. J. Beebe, G. A. Mensing, G. M. Walker, "Physics and applications of microfluidics in biology", Annual Review of Biomedical Engineering, Vol. 4, Aug 2002, pp. 261-286.

[2] J. Voldman, M. L. Gray, M. A. Schmidt, "Microfabrication in Biology and Medicine" Annual Review of Biomedical Engineering, Vol. 1, Aug 1999, pp. 401-425.

[3] P. Dario, M. C. Carrozza, A. Benvenuto and A. Menciassi, "Micro-systems in biomedical applications", Journal of Micromechanics and Microengineering, Vol. 10, 2000, pp. 235–244.

[4] Dong-Sing Wuu, Ray-Hua Horng, Chia-Chi Chan, Yih-Shing Lee, "Plasma-deposited amorphous silicon carbide films for micromachined fluidic channels", Applied Surface Science 144–145, 1999, pp. 708–712.

[5] K. Richter, M. Orfert, S. Howitz, S. Thierbach, "Deep plasma silicon etch for microfluidic applications", Surface and Coatings Technology, 116–119, 1999, pp. 461–467.

[6] J. N. McMullin, "Laser fabrication of integrated microfluidic/micro-optic systems", Proceedings of ICAPT2000, International Conference on Applications of Photonics Technology, Quebec City, June 12-16, 2000, pp. 1050-1055.

[7] J. R. Anderson, D. T. Chiu, R. J. Jackman, O. Cherniavskaya, J. C. McDonald, H. Wu, S. H. Whitesides, and G. M. Whitesides, "Fabrication of Topologically Complex Three-Dimensional Microfluidic Systems in PDMS by Rapid Prototyping", Analytical Chemistry, Vol. 72, No. 14, 2000, pp. 3158 – 3164.

[8] S. B. Cheng, "Exploring design and detection issues for automated multichannel microfluidic immunoassay systems", Doctoral thesis, Department of Chemistry, University of Alberta, Canada, 2001.

[9] P. Friis, K. Hoppe, O. Leistiko, K. B. Mogensen, J. Hubner, and J. P. Kutter, "Monolithic integration of microfluidic channels and optical waveguides in silica on silicon", Applied Optics, Vol. 40, No. 34, December 2001, pp. 6246-6251.

[10] A. Grundmann, "Detecting fluorescent microparticles with the computer-controlled photomultiplier tube R2949 from Hamamatsu Corporation", Internship Report, University of Applied Sciences Berlin, Germany, 2001.

[11] J. N. McMullin, H. Qiao, S. Goel, A. Grundmann, "Optical detection system for biochips using plastic fiber optics", Review of Scientific Instruments, Vol. 74, No. 9, 2003, (to be published).

[12] N. Chiem, L. L.-Shultz, P. Andersson, C. Skinner, D. J. Harrison, "Room temperature bonding of micromachined glass devices for capillary electrophoresis", Sensors and Actuators, B 63, 2000, pp. 147-152.

[13] R. H. Doremus, "Exchange and diffusion of ions in glass", Journal of Physical Chemistry, Vol. 68, No. 8, August 1964, pp.2212-2218.

[14] T. Izawa and H. Nakagome, "Optical waveguide formed by electrically induced migration of ions in glass plates", Applied Physics Letters, Vol. 21, No. 12, December 1972, pp. 584-586.

[15] T. Findakly, "Glass waveguides by ion exchange: a review", Optical Engineering, Vol. 24, No. 2, March/April 1985, pp. 244-250.

[16] A. Brandenburg, "Stress in ion-exchanged glass waveguides", Journal of Lightwave Technology, Vol. LT-4, No. 10, October 1986, pp. 1580-1593.

[17] H. J. Lilienhof, E. Voges, D. Ritter and B. Pantschew, "Field-induced index profiles of multimode ion-exchanged strip waveguides", IEEE Journal of Quantum Electronics, Vol. QE-18, No. 11, November 1982, pp. 1877-1882.

[18] G. H. Chartier, P. Jaussaud, A. D. de Oliveira and O. Parriaux, "Optical waveguides fabricated by electric-field controlled ion exchange in glass", Electronics Letters, Vol. 14, 1978, pp. 132-134.

[19] A. Tervonen, S. Honkanen and M. Leppihalme, "Control of ion-exchanged waveguide profiles with Ag thin-film sources", Journal of Applied Physics, Vol. 62, No. 3, August 1987, pp. 759-763.

[20] S. I. Najafi, P. G. Suchoski and R. V. Ramaswamy, "Silver film-diffused glass waveguides: diffusion process and optical properties", IEEE Journal of Quantum Electronics, Vol. QE-22, No. 12, December 1986, pp. 2213-2218.

[21] M. C. Page, R. Oven, D. G. Ashworth, "Scaling rules for glass based planar optical waveguides made by field assisted ion diffusion", Electronics Letters, Vol. 27, Issue 22, 24 Oct. 1991, pp. 2073–2076.

[22] Ricky W. Chuang, Chin C. Lee, "Low-loss deep glass waveguides produced with dry silver electromigration process", IEEE Journal of Lightwave Technology, Vol. 20, No. 8, August 2002, pp.1590-1597.

[23] J. L. Coutaz and P. C. Jaussaud, "High index gradient in glass by ion exchange", Applied Optics, Vol. 21, No. 6, March 1982, pp. 1063-1065.

[24] S. Honkanen and A. Tervonen, "Experimental analysis of Ag+-Na+ exchange in glass with Ag Film ion sources for planar optical waveguide fabrication", Journal of Applied Physics, Vol. 63, No. 3, February 1988, pp. 634-638.

[25] Armin Grundmann, "Integrating ion-exchanged waveguides and glass microchannels on a single chip to enable optical detection of fluorescent microparticles", Diploma thesis, University of Applied Sciences Berlin, Germany, 2001.

[26] R. G. Walker, C. D. Wilkinson, and J. A. H. Wilkinson, "Integrated optical waveguiding structures made by silver ion-exchange in glass. 1: The propagation characteristics of stripe ion-exchanges waveguides; a theoretical and experimental investigation", Applied optics, Vol. 22, No. 12, June 15, 1983, pp.1923-1928.

[27] S. Honkanen, A. Tervonen, H. von Bagh and M. Leppihalme, "Ion exchange process for fabrication of waveguide couplers for fiber optic sensor applications", Journal of Applied Physics, Vol. 61, No. 1, January 1987, pp. 52-56.

[28] A. Belkhir, "A comparative study of silver diffusion in a glass substrate for optical waveguide applications", IEEE Journal of Quantum Electronics, Vol. 35, No. 3, March 1999, pp. 306 -311

[29] James E. Shelby, "Introduction to glass science and technology", the Royal Society of Chemistry, 1997.

[30] B. G. Pantchev, "One-step field-assisted ion exchange for fabrication of buried multimode optical strip waveguides", Electronics Letters, Vol. 23, 1987, pp. 1188-1190.

[31] H. Zhenguang, R. Srivastava and R.V. Ramaswamy, "Single-mode buried channel waveguides by single-step electromigration technique using silver film", Applied Physics Letters, Vol. 53, No. 18, October 1988, pp. 1681-1683.

APPENDIX 1: PROCEDURE OF FABRICATING MICROCHANNELS

Microchannel etching processes were facilitated by the Micromachining and Nanofabrication Facility (NanoFab) in the University of Alberta and Micralyne Inc. of Edmonton. The detailed sequence of preparing the cover plate, cleaning and bonding steps presented below was achieved with the help of Dr. Justine Taylor in the Harrison group in the Chemistry Department at University of Alberta, Dr. Yuebin Ning from Norcada Inc. of Edmonton, and the NanoFab staff. Corning 0211 glass and Schott Borofloat glass were used as the substrates and the cover plates.

I. Etching microchannels

1. Label substrate

Label substrates by numbers at a corner of the substrate backside with a diamond scriber before any process to distinguish each substrate from the others and the front side from the backside. It is especially important for Schott Borofloat glass because it has different characteristics at each side. Glass etching can only be carried out on the specific side, which is usually labeled during manufacture. Corning 0211 substrates don't distinguish between sides.

In the following processes, substrates should be positioned coherently by pointing the numbers to the same direction. This is helpful for comparison experiments when a batch of substrates are applied with slightly changed processes. For example, if something goes wrong, one can use the identical position of substrates to figure out that the reason is due to the change of the process or simply the nonuniformity of processing over one whole substrate.

2. clean substrate

Cleanliness of substrates is rigidly required before they are coated with metal or photoresist. The size of dust, grease and other contamination on the substrates are usually bigger than the thin film coated, so that the adhesion of

thin films to substrates is reduced, and pin-holes are generated in the subsequent processes, resulting in defects in the device.

NanoFab Hot Pirahna (H_2SO_4: H_2O_2 = 3: 1, 90-110°C, 15 min) bath shown in Figure A1-1 is proved sufficient to remove organic and loose particles on the substrates, followed by a dump rinsing for 5 cycles. Protect the operator with rubber apron, mask and heavy duty gloves. Use glass beakers and Teflon sample holder: A92-40M for 4x4 inch substrates in the Piranha bath. The sides to be sputtered face down, which helps to drop off particles from substrates. Dry full-size substrates in the spin rinse dryer (rinse 60s, dry 240s) in Figure A1-2, or dry smaller substrates with a Nitrogen gun. The next step after Piranha always needs to be processed as soon as possible; otherwise, substrates will be recontaminated after a few hours.

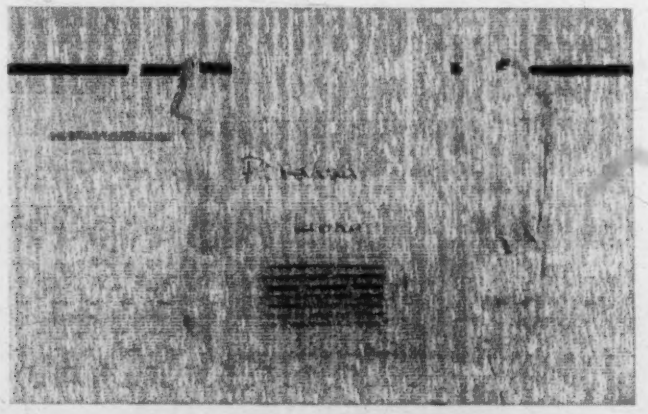

Figure A1-1 Hot piranha bath

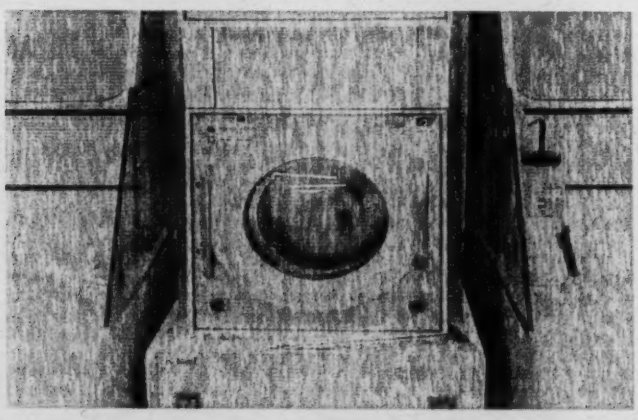

Figure A1-2 Spin rinse dryer

If the glass is going to be metallized in the Micralyne Inc., follow Micralyne cleaning procedure.

3. Metallize glass

In the NanoFab, 30 nm Chromium (Cr) and 190 nm gold (Au) are sputtered using Lesker sputtering machine "Bob" (Figure A1-3) using the following parameters: for Cr, gun 1 (low position), base pressure $2.0*10^{-6}$ Torr, sputter pressure $7.0*10^{-3}$ Torr, power 300 W, burn in 3 min, sputter time 6 min; for Au, gun 2 (high position), base pressure $2.0*10^{-6}$ Torr, sputter pressure $7.0*10^{-3}$ Torr, power 75 W, burn in 1 min, sputter time 18 min.

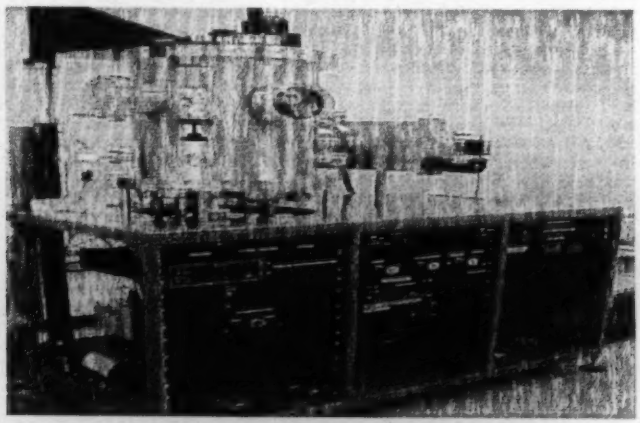

Figure A1-3 Lesker sputtering machine "Bob"

In Micralyne Inc., glass substrates are cleaned and then removed a-few-nm glass by radio frequency (RF) etching, before a 40 nm Cr (Our etching result indicates 20 nm.) and a 100 nm Au (Our etching result indicates 230 nm.) Au films are sputtered. The glass etching results using the above facilities are discussed in Section 2.3.1.

4. Lithography

HPR 504 photoresist is used to generate channel patterns and also as another protective layer for glass etching. Without photoresist, Au will be gradually attacked by the glass etchant, starting from the defects on the metal films. To remove loose particles picked up from the sputtering machine, clean the substrate with sufficient acetone, isopropyl alcohol (IPA), and nitrogen blow while it is spinning on the Solitec spinner (Figure A1-4).

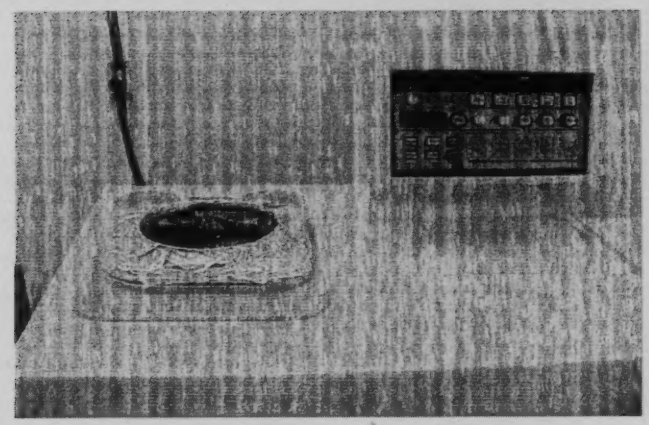

Figure A1-4 Solitec Spinner

The photoresist thickness changes with spin speed, temperature, humidity, and substrate type. The NanoFab standard process of HPR 504: spread 10 s 500 rpm, spin 40 s 4000 rpm; prebake in oven 115°C, 30 min; rehydrate in room temperature, 30 min; UV exposure 4 s (Figure A1-5); micropoint 354, develop 10-14 s, used to generate a 1.2 μm photoresist, but only 650-800 nm recently. Developing time also varies with the photoresist thickness, the temperature and humidity of the environment. Always check the developing result with a microscope and measure photoresist thickness with the Tencor Alpha Step profilometer, in Figure A1-6.

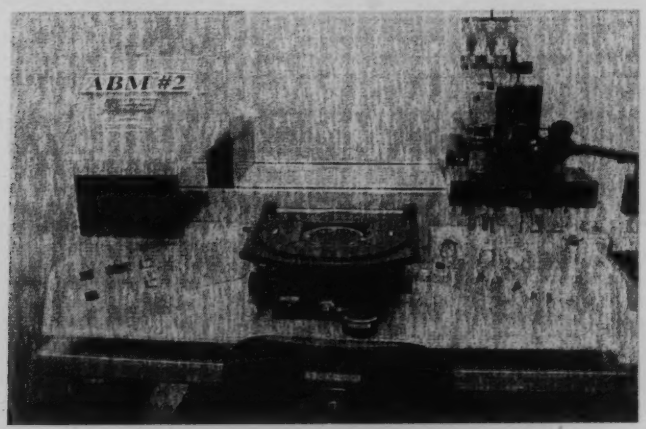

Figure A1-5 ABM Exposure and maskaligner

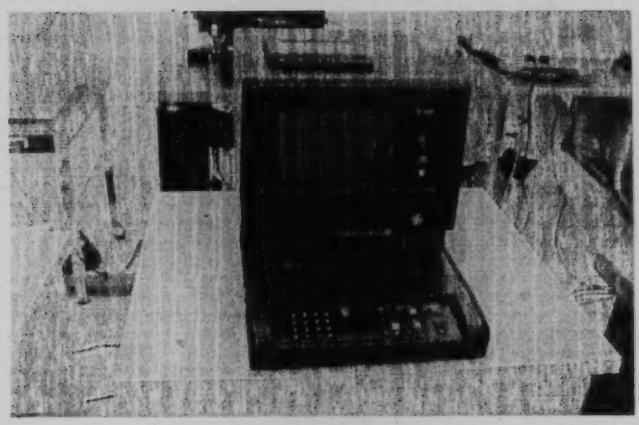

Figure A1-6 Tencor Alpha Step profilometer

Interference patterns indicating different thickness of the photoresist have to exist since the round trunk of the spinner doesn't accept heterogeneous shape substrates well. The photoresist reflecting pink light is thicker than where green light is reflected. As a result, the developing is not even throughout the whole substrate. This effect is more obvious at the corners. Features should have been avoided at the corners when masks were designed.

5. Etch Au and Cr

The NanoFab standard wet deck process uses Au etchant (HI/KI) and Cr etchant (Ceric ammonium nitrate). The Cr where it is etched turns black and dissolves in the etchant gradually. The features are then exposed and the substrate can be seen through.

6. Etch glass

Glass is etched using the NanoFab recipe, hydrofluoric acid (HF) / nitric acid (HNO_3) / H_2O (20:14:66). Extra protective gear including rubber apron, mask and heavy duty gloves are used during glass etching. Use plastic beakers and a metal rod to hold the sample holder (Figure A1-7). Glass etchant is put on a magnetic plate and agitated by a magnetic stirrer at a modest speed (speed 2). The etching rate is approximately 1.6 μm /min on corning 0211 glass and 0.5 μm/min on Schott Borofloat glass. Black tape is used to protect the backside of the substrate from etching.

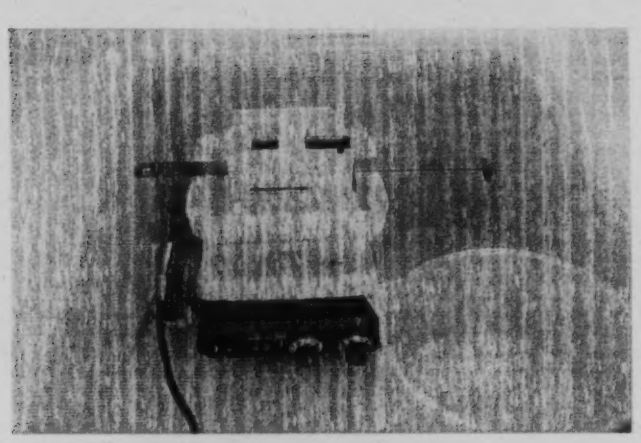

Figure A1-7 Glass etching setup

7. Remove PR and metals

Photoresist is then removed by acetone, and both metals are removed using standard etchants. The bottom substrate is ready for bonding.

II. Preparation of the cover plate

The cover plate is marked with a waterproof marker where via holes will be drilled, corresponding to the reservoir positions on the bottom plate. We use a drill press (Dremel Model 285 T6) with a 2 mm diameter diamond drill bit, in Figure A1-8. On a hot plate (OK Industries SA-750), microscope slides are glued with CrystalBond™ 509 (flow point 77°C) to both sides of the glass substrate for protection against glass chipping or scratching during drilling.

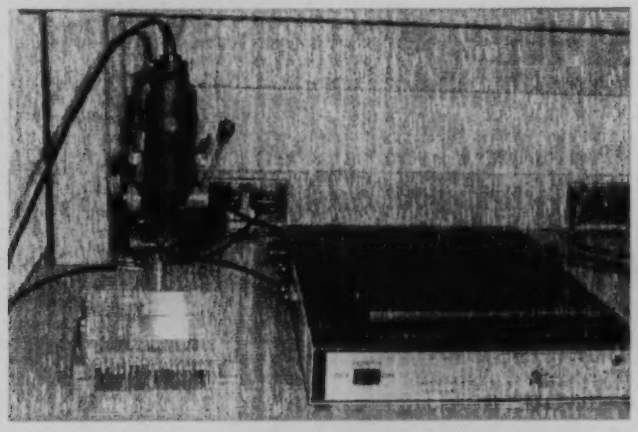

Figure A1-8 Drill press, drill bit and hot plate

Glass has to be immersed in cooling water during drilling, to reduce stress caused the increasing temperature. Set up the motor at the speed of 15,000 rpm. Move down the lever of the drill press steadily. Because Crystalbond is a softer substance than glass, we can feel it when the drill bit drills through one layer of glass and meets Crystalbond. Crystalbond also serves as a buffer between two layers of glass so that the impact on the cover plate is reduced at the moment when glass is drilled through. The third layer shouldn't be drilled through, otherwise chipping may happen at the via hole bottom when the drill bit suddenly drills through the third glass and comes into water.

After the holes are drilled, the microscope slides can be taken away by heating up again on the hot plate. Acetone followed by a hot or cool Pirahna bath is used to clean the CrystalBond residue on the cover plate.

III. Bonding the cover plate with the bottom substrate

1. Hot pirahna bath

A standard hot pirahna bath for 15min removes organic impurity and loose particles. The to-be-bonded sides of the substrates face down to facilitate particles leaving the surfaces. Rinse the substrates in the dump for 5 circles. Dry full-size substrates in the spinning rinsing dryer or small substrates by a nitrogen gun.

2. Scrubbing with detergent

Tape each substrate on its backside in the center of a high-pressure washer (HPW) mounting ring by a blue bonding tape, Figure A1-9. Scrub the front side of each substrate with a sponge using the NanoFab-made detergent solution for 3 min to remove stubborn particles.

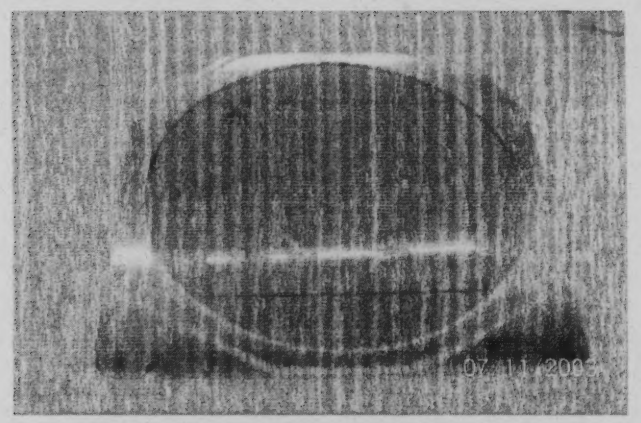

Figure A1-9 Substrate is taped in the center of HPW mounting ring with a bonding tape.

Lean the substrates on a sample holder in the dump, with scrubbed surfaces facing outside. Run 5 circle rinsing for three times. Take out the cover plate, and hold the mounting ring with the front side of the substrate facing down at 45°. Use a nitrogen gun to blow the back side roughly first, and then starting from a corner of the front side, move slowly to the other corners, blowing constantly towards one direction to avoid water moving back and forth to recontaminate the glass surface.

After the cover plate is dried, put it on a sample holder with the front side facing down. Then work on the bottom substrate.

3. Initial bonding

Insert a clean mounting ring under the cover plate as a spacing to separate the cover and bottom substrate before initial bonding. Then the bottom substrate is put under the other two mounting rings with the front side facing up. See the schematic diagram in Figure A1-10.

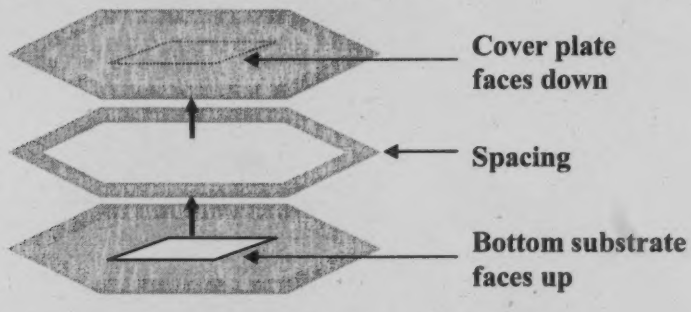

Figure A1-10 schematic diagram of initial bonding

Slide the cover plate on the spacing ring to align the via-holes with the reservoirs on the bottom substrate. A microscope can be used to assist a more accurate alignment. When a good alignment is achieved, starting from one corner, press the two substrates together across the diagonal and also towards the other two corners. Squeeze the substrates hard enough to push the air out. Remove blue tapes and all the mounting rings. Inspect the bonding result. A diligent cleaning should result very few Newton rings, which indicates the existence of particles on the bonding surface. If there are serious Newton rings, the substrates need to be taken apart under water and repeat from Step 2.

4. Post bake

Put bonded substrates in the oven with a steel block on the top to add weight. Bake at 300°C for 3 hours, followed by a natural cooling down.

IV. Cutting, polishing

Bonded substrates can be cut using a diamond-dicing saw in Micralyne Inc. or a programmable water-jet cutting machine in the machine shop of the Department of Electrical and Computer Engineering at University of Alberta. If using the latter, protective layers need to be glued on the both sides of the bonded substrates using Crystalbond, because the approximated 200-μm-diameter abrasive the water-jet uses scratches any surface contacted. After cutting, the edges are polished in the machine shop using a sophisticated polishing process. The polishing result is as fine as 1 μm.

When polishing is finished, protective layers are taken away. Acetone and a piranha bath are again used for cleaning. The enclosed microchannels are ready for the applications of microfluidics.

APPENDIX 2: PROCEDURE OF FABRICATING ION-EXCHANGE WAVEGUIDES

All the processes except the ion exchange and dicing were carried out using the facilities available at the NanoFab in the University of Alberta with the assistance of the NanoFab staff. Corning 0211 glass 4x4 inch (0.021 inch thick), Schott Borofloat glass 4x4 inch (0.044 inch thick), and smaller pieces cut from the full size glass above are used as the substrates.

1. Label substrates

Label substrate on the backside of the substrates, as stated in Appendix 1.

2. Clean substrates

Cleanliness of substrates is again rigidly required before sputtering. NanoFab Hot Pirahna (H_2SO_4: H_2O_2 = 3: 1, 90-110°C, 15 min) bath is used.

3. Sputter Cr

Aluminum, Au, Ti, and Cr are tested as the ion-exchange mask layer in the earlier research of our group. Among them, using Cr decreases the complication of multi-metal etching later on, and Cr is a well-accepted ion-exchange mask in the literature. Chromium sputtering is calibrated on the Lesker sputtering machine "Bob" in Figure A1-3. The following parameters: gun 2 (high position), sputter pressure $7.0*10^{-3}$ Torr, base pressure $2.0*10^{-6}$ Torr, burn in 3 min, power 300 W, and sputter time 35 min, give approximately 500-nm-thick Cr film.

Rectangular sample holders are used to cover substrate edges to prevent electrical shorting during ion exchange. For substrates not fit in the sample holder, cover the edges of substrates with a thick waterproof marker, which can be removed by IPA later. The holder positions are shown in Figure A2-1. The maximum sputter thickness is at radius 9 to 10 cm, which is very close to the centers of the 4x4 inch substrates. By this arrangement, metal film thickness has the best distribution, the variation of which across the substrate is about 15% [R25]. When attaching substrates to the rotating plate, avoid holes on the rotating plate, through which Cr will be sputtered on the backside of substrates.

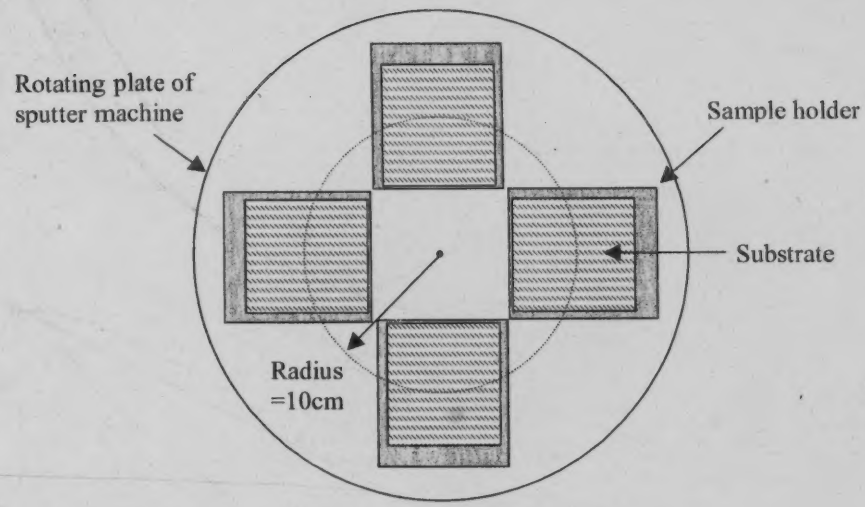

Figure A2-1 Optimum sample holder positions

4. Lithography

HPR 504 is usually used as the photoresist to generate the desired waveguide structure. To remove loose particles picked up from the sputtering machine, clean the substrate with sufficient acetone, IPA, nitrogen gun while it is spinning on the Solitec spinner. Also, the beaker and photoresist it contains need to be clean and free of particles. Pour the PR into the clean beaker slowly, and let it sit covered for half an hour to dismiss the air bubbles trapped in photoresist. Air bubbles can cause pinholes in the Cr layer when etching the Cr so that Ag can migrate into the substrate through the pinholes.

Apply, bake, expose, and develop photoresist following the standard NanoFab procedure, as described in Appendix 1.

5. Etch Cr

Following lithography, Cr etching is conducted using the standard process in NanoFab, also interpreted in Appendix 1.

6. Remove photoresist

Before sputtering Ag on the top of Cr, photoresist needs to be removed completely; otherwise, photoresist residue is buried under Ag layer and decomposes at ion-exchange temperature to form bubbles that can devastate the waveguides. An Acetone base (5 min), a photoresist remover 1165 base on the hot

plate (60°C, 5 min), and a DI water base are set in the fumehood to remove the majority of photoresist (Figure A2-2). Then a cool Piranha bath (<45°C, 10 min) is carried out on the wetdeck to remove the remaining photoresist. Piranha is an efficient solvent of organic material. As hot piranha (90-110°C) attacks most metals including Cr, cool piranha lower than 45°C is used to remove the photoresist but safe to Cr. After the entire above, photoresist residue is still visible most of the time, especially trapped around the area where there are openings.

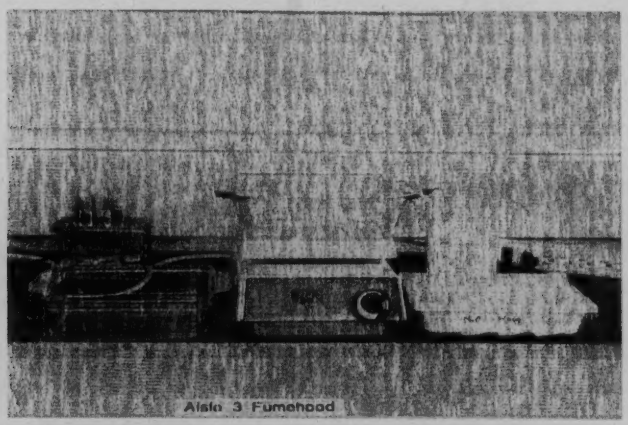

Figure A2-2 An acetone base, a photoresist remover 1165 base on the hot plate and a DI water base are set in the fumehood to remove photoresist

7. Heat up substrates

Substrates are heated in a Minibrute furnace (Figure A2-3) with the following settings: center 160, back 150, front 850, 10 min, and the back of the furnace open. Lay the substrate on a crystal cart with the Cr layer facing up, as shown in Figure A2-4, before putting it into the furnace. The temperature in the furnace reaches 380-400°C at which temperature the photoresist decomposes and burns off. At the same time Cr is oxidized into Cr_2O_3. Substrates are a little bent with edges up after taken out of the furnace due to the thermal tension. An additional cool Piranha (<45°C, 10 min) is applied to remove contaminating particles from the furnace and the bumps around the mask openings, as described in Section 2.1.3.1.

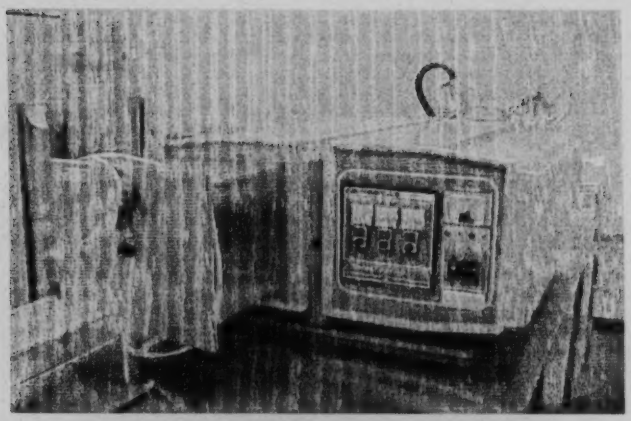

Figure A2-3 Minibrute furnace

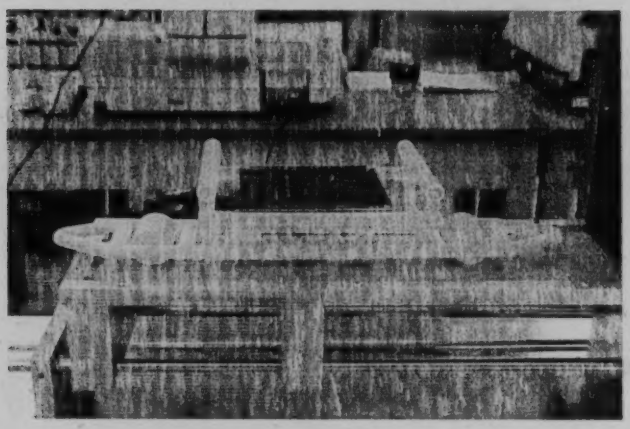

Figure A2-4 lay substrate on a crystal cart with the Cr layer facing up at the entrance of the furnace

8. Sputter Ag and Au on front

Silver thickness should be chosen large enough so that it is not used up during ion exchange. The depletion of Ag can cause waveguide surface defects. Experiments prove that a 1.5-μm-thick layer of Ag can generate waveguides up to 60 μm deep. The following sputter parameters are used to sputter 1.5 μm Ag: gun 2 (high position), base pressure $2.0*10^{-6}$ Torr, sputter pressure $7.0*10^{-3}$ Torr, burn in 3 min, power 300 W, sputter time 37.5 min.

Gold is sputtered as a cover layer on the top to protect Ag and ensure electric conductivity. The following sputter parameters are used to achieve 1 μm Au: gun 1 (low position), base pressure $2.0*10^{-6}$ Torr, sputter pressure $7.0*10^{-3}$ Torr, burn in 1 min, power 75 W, sputter time 128 min.

On the backside, sputter Ag as an electrode. Silver, Al and Au were tested in the earlier experiments in our group, proving that a silver layer on the backside ensures the least deterioration. Silver thickness was chosen as high as on the front to reduce warping due to thermal expansion. The same putter parameters as the front. In all the above sputtering processes, rectangular sample holders are used for full-size substrates and positioned as in Figure A2-1.

9. Ion exchange process

The apparatus and the diagram of the ion exchange process are described in Figure A2-5 and A2-6.

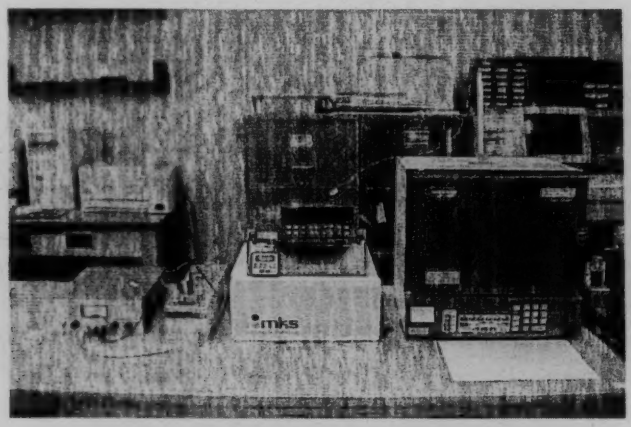

Figure A2-5 Apparatus of the ion exchange process

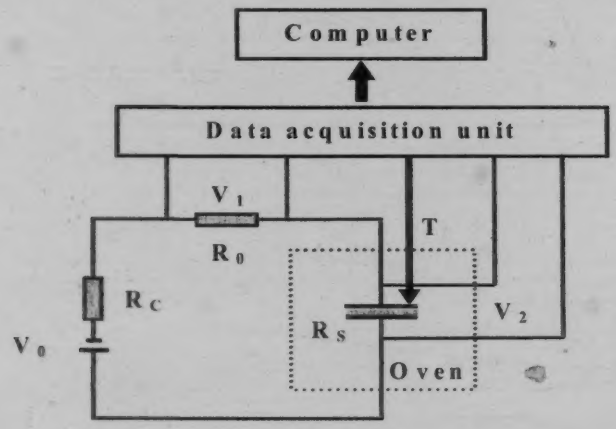

Figure A2-6 Diagram of ion exchange process

A power supply V_0 (Harrision 7207B DC), its resistance R_C (a few Ohms), and a resistor R_0 (1433-K decade resistor) are put in series with the glass

substrate. R_0 is chosen 3 decades smaller than the substrate resistance, so that V_1 is negligible compared with V_2. In the oven (Omegalux LMF-6525), the glass substrate is held between two electrodes that make contact at several points on each side. The thermocouple is attached to the chip to monitor the temperature T. The current through the substrate is monitored by the voltage V_1 over R_0. V_1, V_2 and T are recorded simultaneously by the data acquisition unit (Fluke Hydra) and exported to the computer.

Temperatures (280-400°C) and applied electric fields (35-285 V/mm) are used on a wide range of substrates. In an example on a 0.021-inch-thick Corning 0211 substrate, setting V_0 19 V, R_0 1 Ω and the oven 400°C, 40-min ion-exchange generate approximately 30 μm waveguide.

10. Etch Au, Ag and Cr_2O_3

Standard Au etchant (HI/KI) is used to remove Au and Ag, as Au etchant attacks Ag as well. Standard Cr etchant on a hot plate (Ceric ammonium nitrate, 50°C) is used for Cr_2O_3 etching. Cr etchant attacks Ag as well.

11. Dice, polish and prepare substrates for SEM and waveguide loss measurement

We can carry on the whole piece of substrates to integrate microchannels and bond the substrates, or dice the substrates to smaller pieces for waveguide loss measurements and testing. We send the substrates to Micralyne inc. to dice them using a diamond saw. To prepare a SEM sample, usually a size of approximately 1x1 cm is cleaved using a diamond scriber from the backside of the substrate. To measure the waveguide loss, we polish the ends of waveguides using a serial of sandpapers from rough (a-few-ten μm) to fine (1 μm).

APPENDIX 3: A DUAL FUNCTIONAL MASK LAYOUT

Waveguide and microchannel patterns were designed on a 4x4 inch positive quartz mask. The layout, as shown in Figure A3-1, consists of four major parts (a)-(b) from left to the right, and four types of intersections (A)-(D). 250-μm-wide dicing marks are designed to assist dicing the whole substrate into 2x3.5 cm^2 chips. Four identical alignment marks are put at the corners of the mask to assist the alignment of waveguide and microchannel patterns. The actual working area on the mask is 8x8 cm^2. An approximately 1-cm margin at each side is left for handling.

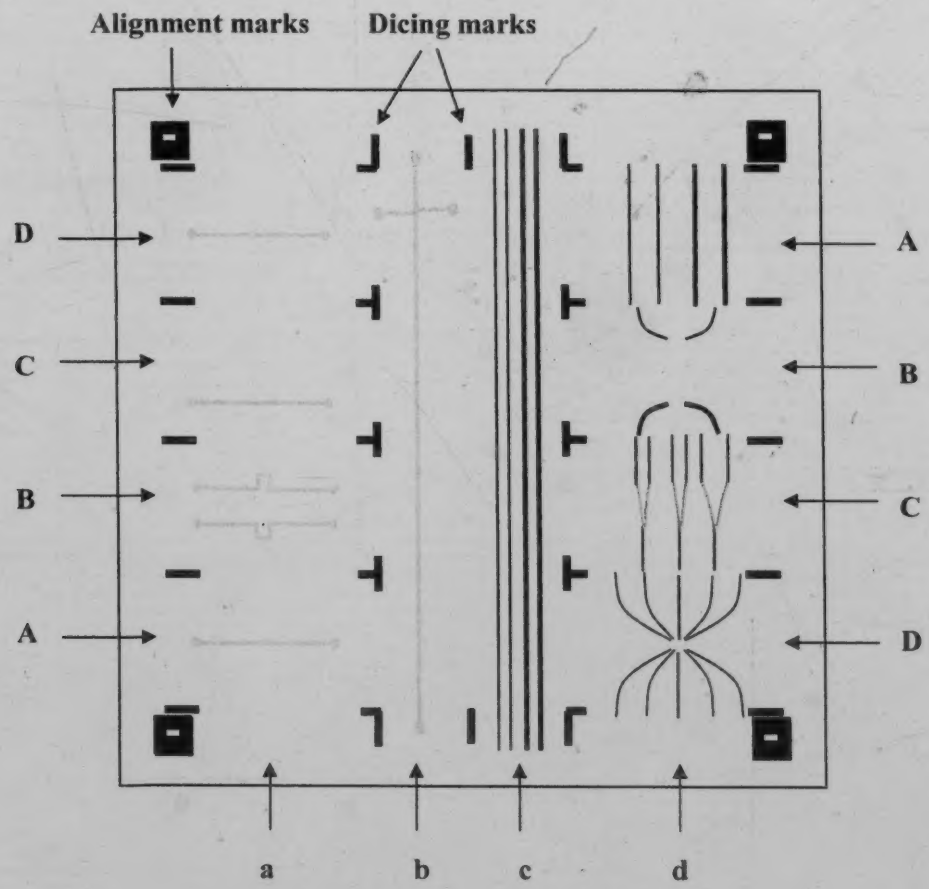

Figure A3-1 Layout of the dual functional mask

Part (a): 20-μm-wide 2-cm-long microchannels with 1-mm-diameter reservoirs at the two ends. These microchannel patterns are designed to integrate

with waveguide patterns or used individually to fabricate microchannels for flow driven experiments.

Part (b): 20-μm-wide cross shape microchannels with one 8.5-cm-long channel intersected with two 0.5 cm short channels on each side with 100 μm mismatched intersections, which is called a "double T" structure. This design allows for formation of geometrically defined plugs of solution. 1-mm-diameter reservoirs are designed at every channel end.

Part (c): four 9-cm-long waveguide 200 μm apart from each other with two kinds of width, 10 μm and 20 μm for each two of them. The long waveguide patterns are designed for waveguide loss measurements. The half-cm waveguides sticking out at each end will be diced off along the dicing marks and can be used for SEM tests.

Part (d): four groups of short waveguides with 10 and 20 μm width. They are designed to integrate with microchannels in Part (a), and also to be fabricated into individual chips for waveguide property tests or demonstrations.

Intersection (A): four straight waveguides with 10 and 20 μm width for each two of them intersecting a straight microchannel. This is the simplest intersection structure. One disadvantage is that the input light may shine directly into the output waveguides and increase the background noise.

Intersection (B): curved waveguides with a 10 or 20 μm width for each side intersecting the U-shape microchannels with 1x2 mm^2 U cells. A ¼ circular waveguide directs light into one end of the U cell. On the other end of the U cell, the other ¼ circular waveguide picks up the fluorescence from the fluids in the U cell.

Intersection (C): three 10 μm Y-shape waveguides intersecting a straight microchannel. The light is directed into a Y-shape waveguide form one light source and shines at different places in the microchannel, or fluorescence signals from different places of the microchannel are detected by a Y-shape waveguide and eventually by one detector. One application of this structure is to measure the flow speed.

Intersection (D): eight 10 μm waveguides distributed 20° apart around a 500-μm-diameter circular chamber in the center of a straight microchannel. The reaction of the solutions in the chamber can be studied exclusively from different angels.

In the processing, unwanted features can be simply blocked by black tape on the backside of the mask. The mask can be cleaned with acetone after the tape is taken off. For example, we fabricate waveguides first on a substrate using the Part (c) and (d) of the mask. When we make microchannels on the same substrate, the mask is covered by black tape except Part (a) and then rotated by 180° to align with the waveguides with Part (d) patterns on the substrate. The microchannels with the Part (a) patterns are etched to intersect the corresponding waveguides on the substrate, leaving the waveguides with the Part (c) patterns untouched.

In some experiments, we used the whole mask for the waveguide fabrication, and then etched microchannels by rotating the mask 180° and protecting the middle two parts by taping the mask. As a result, Intersection (A)-(D), as well as their mirror images, were formed on the same substrate. The mirror images of Intersection (A)-(D) are the waveguides with Part (a) patterns intersected with the microchannels with Part (d) patterns. They cannot be used in the microfluidics experiments, but they can be used for analyzing the intersections of waveguides and microchannels, as we already did.